JOURNAL OF GEOPHYSICAL RESEARCH, VOL. ???, XXXX, DOI:10.1029/,

Very High Altitude Aurora Observations With The Solar Mass Ejection Imager

D. R. Mizuno,[1] A. Buffington,[2] M. P. Cooke,[3] C. J. Eyles,[3] P. P. Hick,[2] P. E. Holladay,[4] B. V. Jackson,[2] J. C. Johnston,[4] T. A. Kuchar,[1] J. B. Mozer,[4] S. D. Price,[4] R. R. Radick,[4] G. M. Simnett,[3] D. Sinclair,[4] S. J. Tappin,[3] D. F. Webb[1]

D. R. Mizuno, Institute for Scientific Research, St. Clement's Hall, 140 Commonwealth Avenue, Chestnut Hill, Massachusetts, 02467-3862 (Don.Mizuno@hanscom.af.mil)

[1] Institute for Scientific Research, Boston College, Chestnut Hill, Massachusetts, USA

[2] CASS, University of California at San Diego, California, USA

[3] School of Physics and Astronomy, University of Birmingham, UK

[4] Air Force Research Laboratory, Space Vehicles Directorate, Hanscom AFB, Massachusetts, USA

Abstract. The Solar Mass Ejection Imager (SMEI) is a sensitive scanning instrument mounted on the Coriolis satellite which assembles an approximately all-sky image of the heliosphere in red-biased visible light once per orbit. Its lines of sight pass obliquely through the topside ionosphere and magnetosphere. We present serendipitous observations of a visual phenomenon detected at high altitudes ($\geq$ 840 km) over the auroral zones and polar caps. The phenomenon is observed in two basic forms. The first, and more common, are periods of brief (1–3 minutes), nearly uniform illumination of the imager's field of view, which we interpret as transits of the satellite through a luminous medium. The second appear as localized filamentary structures, which we interpret as columns of luminous material, viewed from a distance, possibly extending to visible altitudes of 2000 km or higher. More than 1000 occurrences of these phenomena were recorded during the first full year of operations. These observations are well correlated in brightness and frequency with periods of enhanced geomagnetic activity.

1. Introduction

Visual atmospheric phenomena at very high altitudes (> 800 km) have been sporadically reported. There have been astronaut reports of auroral light as high as 1000 km (e.g. *Jackson et al.* [1992]), although astronauts generally have observed the aurora at or below the space station and shuttle orbits at ∼300 km.

The aurora is usually brightest during geoactivity, e.g., geomagnetic storms or substorms, within the auroral ovals where electrons stream down field lines open to the solar wind. The optical aurora extends from a base of ∼100 km above the Earth's surface to heights of 400–500 km [*Akasofu* 1998], but the upper boundary is uncertain.

Carl Størmer [1955], in his long study of the aurora, occasionally observed high sunlit rays, at altitudes greater than 700 and as high as 1100 km, during very intense geomagnetic storms. The visibility of these rays has been attributed to resonant scattering of sunlight from N_2^+ molecular ions (*Hunten* [2003] provides a concise summary, along with references therein). More recently, *Romick et al.* [1999] have reported the first direct observations of N_2^+ spectral line emission at high altitudes (up to 900 km), during a period of only moderately elevated geoactivity, with the UVISI spectrographic imagers on the Midcourse Space Experiment (MSX) satellite.

The Solar Mass Ejection Imager (SMEI) experiment [*Eyles et al.*, 2003; *Jackson et al.*, 2004] was designed to observe and obtain time sequences of heliospheric phenomena propagating from the Sun and in interplanetary space, such as coronal mass ejections (CMEs) and corotating structures. The strategy for this objective is to image a large fraction of the entire heliospheric sky at the cadence of the 102-minute orbital period, with sufficient sensitivity and photometric stability to detect faint disturbances against the much brighter stellar and zodiacal background. SMEI has achieved success in this primary objective, with ∼100 CMEs having been observed in the first year of operations, and also has demonstrated the ability to detect Earth-directed CMEs ∼1 day in advance of arrival [*Tappin et al.*, 2003].

The observing strategy developed for this purpose, involving the sky coverage and cadence, the orientation of the imagers, their sensitivity, and the satellite's polar orbit, also make this instrument useful in surveying the topside ionosphere for evidence of optical phenomena during geomagnetic disturbances.

The presence of N_2^+ at optically detectable column densities at very high altitudes has generally been attributed to molecular upflow or outflow from the ionosphere, which has been detected with in situ mass spectrometers (e.g. *Taylor* [1974], *Yau et al.* [1993]). With this interpretation of optical phenomena at high altitudes, the current observations, a portion of which show structures possibly extending to 2000 km or higher, may be useful in studying the morphology of this process.

In Section 2 we explain details of the SMEI instrument and the geometry of the cameras' field of view over the polar regions. In Section 3 the data set is presented, and the SMEI aurora observations are described. In Section 4 an interpretation of the observations is offered, including a consideration of the physical origin and a discussion of the structures responsible for the phenomenon.

2. Instrumentation and Viewing Geometry

SMEI was launched on the US Air Force Space Test Program Coriolis satellite on 6 January 2003. The satellite is in a sun-synchronous, circular polar orbit at an altitude of

840 km. The orbit is maintained approximately over the terminator; the satellite ascends on the dusk side and descends on the dawn side. The declination of the orbit axis, in Earth-centered inertial coordinates, is fixed at approximately $-8°$, and so, for the north polar passage, the orbit inclination ranges from 31° sunward of the terminator, at the summer solstice, to 15° on the nightside at the winter solstice. The situation is reversed for the south polar passage.

The sensor suite consists of three carefully baffled CCD cameras each covering a narrow strip of the sky approximately $3° \times 60°$ in size. The cameras are mounted on the satellite with their fields of view aligned end-to-end, and slightly overlapping, so that the total instantaneous field of view is a 3° wide strip extending 150° along an approximate great circle with the ends near the orbit axis. Figure 1a is a schematic of the satellite in orbit, showing the mounting of the cameras and their fields of view. The satellite's attitude is fixed in horizon coordinates, and so the satellite rotates once per 102-minute orbit. For each orbit, the cameras' field of view therefore sweeps out a little less than 4π steradians of the sky, with the gaps being a large circle in the direction of the Sun and a smaller circle in the direction opposite. The unfiltered CCDs have a red-biased spectral response that peaks at ~700 nm and has 50% peak responsivity at approximately 500 and 900 nm.

The center of the $3° \times 150°$ composite field of view is approximately directed opposite to the satellite's velocity vector, to avoid the camera baffles sweeping up contamination. Figure 1b is a schematic of the rearward-facing hemisphere as seen from the satellite, showing the fields of view of the three cameras and the position of the Earth. The cameras' fields of view are tilted about 30° above the local horizontal and about 60° above the Earth's limb, and therefore the lines-of-sight pass obliquely through the topside ionosphere and on through the magnetosphere. Over a given point on the Earth situated along the satellite's ground track, the sampling height is initially 840 km as the satellite passes by, and increases to 2500 km ∼10 minutes later as the oblique field of view advances around the orbit. Figure 1c is a schematic of this geometry. For points away from the ground track, a similar sampling geometry holds, except that the minimum height sampled increases with transverse distance. For points 300 km from the ground track, the minimum viewed height is 1000 km, and at 1200 km distance, the minimum height is 1500 km.

Figure 1d shows the sampling of the topside ionosphere/magnetosphere for a single example orbit. The dotted lines delineate the 600 km wide swath sampled from 1000 km (or below) and higher, and the dashed lines delineate the 2400 km wide region sampled from 1500 km and higher. In each orbit, the topside ionosphere and magnetosphere are sampled from 1500 km and up for nearly half of the polar cap above 60° latitude.

3. The Observations

The primary data product for SMEI is a set of all-sky images, each representing the brightness of the sky over the SMEI passband for a single 102-minute orbit. The instrument operates continuously, so the data set comprises a sequence of orbit images, 14 per day, interrupted only for periodic calibration and diagnostic purposes, and occasionally for software anomalies and telemetry problems.

The choice of projection for representing the entire celestial sphere in two dimensions always involves trade-offs between simplicity of interpretation on the one hand and minimal distortion on the other. The sun-centered equal-area Hammer-Aitoff projection selected for the orbit images [*Calabretta and Greisen*, 2002] provides a reasonably undistorted representation of the sunward hemisphere, where most heliospheric disturbances would be observed, at the cost of more serious distortion around the perimeter of the image region, corresponding to the poles and the antisunward longitudes. An example of an orbit image is shown in Figure 2. The images are oriented in ecliptic coordinates, with a nominal pixel size of 0.5° and a resolution of ∼1°.

3.1. Data collection and image assembly

Each of the three SMEI cameras captures an image of its 3° × 60° field of view every 4 seconds. The pixel size of the CCD array is $\sim 3' \times 3'$, much smaller than the target resolution of 1°, and so to reduce the telemetry rate required, the raw CCD frames are averaged over 4×4 pixel bins before transmission back to Earth. This necessitates an on-board flatfield correction prior to the rebinning. The stored pixel values have a limited dynamic range, and so the raw values, representing 4.7 photoelectrons per digitization unit in each CCD pixel [*Eyles et al.*, 2003], are first scaled by 0.75 to prevent arithmetic overflow as a result of the flatfield correction.

On the ground, the transmitted CCD frames are processed and assembled into the all-sky orbit images. Each orbit comprises about 1500 CCD frames per camera. For each frame, the dark offset and electronic bias are subtracted, and other conditioning is performed such as bad-pixel deletion, spike detection, compensation for geometric effects in the optics, and application of a low-resolution flat field. The processed frames are position-tagged and initially registered and averaged together on a standard grid in fixed sidereal coordinates at approximately the same spatial sampling, $\sim 12'$, as the CCD frames. The pixels in this intermediate representation are then resampled onto the sun-centered Hammer-Aitoff projection, in ecliptic coordinates, at the lower spatial resolution.

The brightness values in the orbit images are not currently converted to physical units, but remain in the 0.75-scaled analog-to-digital conversion units of the transmitted CCD frames. These units, termed ADU, are the brightness units used in this paper. For a comparison, on this scale the Galactic plane has a typical surface brightness, when averaged in 1° bins, and away from bright stars, of about 200 ADU, and a peak brightness, near the Galactic center, of about 1000 ADU.

With all offset and normalization corrections applied, the ADU scale is proportional to the in-band radiance as measured by the SMEI instrument, but the calibration factor to radiance has yet to be determined precisely. The brightness of aurora is typically expressed in Rayleighs, where 1 Rayleigh = $10^{10}/4\pi$ photons $s^{-1}m^{-2}sr^{-1}$. The conversion of ADU to Rayleighs is outlined in Appendix A; we find 1 ADU = 36 Rayleighs with an uncertainty of $\sim$3%.

3.2. Sensitivity and transient object detection

A given point on the sky takes about 1 minute to cross the 3° field of view, and the 1° pixels in the Hammer-Aitoff orbit images are about 5 times larger in linear dimension than the bins in the transmitted CCD frames. Consequently each pixel in the final images is an average of many input values accumulated over 10 or more CCD frames. The typical total RMS noise in a single transmitted CCD frame (after on-board rebinning), combining readout noise and Poisson noise in the lowest background regions, is about 1 ADU, and this is reduced by about a factor of 10 in the composite orbit images. The instrument, with current processing, has a sensitivity that is sufficient to detect objects with surface brightnesses below 1 ADU.

The stellar background and zodiacal light are together far brighter than the faint heliospheric structures that SMEI is designed to detect. A rigorous processing will explicitly remove these backgrounds; these efforts are under development. At present the backgrounds are removed by taking the difference between the image for the current orbit and the image for the preceding orbit. This technique has the advantage of providing a very efficient removal of backgrounds and fixed instrumental artifacts, but requires that the targeted objects move or change sufficiently from orbit to orbit to avoid significant cancellation, and compromises our ability to determine reliable surface brightnesses for the same reason. Brightnesses measured from orbit difference images are, however, lower limits.

While many instances of the high-altitude phenomenon presented here are bright enough to be easily visible in the orbit images without differencing, as Figure 2 demonstrates, the majority are too faint to be identified using the basic images. For the highest sensitivity, and in the interest of a uniform search procedure, the orbit image differencing technique is used throughout to locate and characterize the phenomena, at the expense of somewhat less accurate measures for the brightest examples.

The orbit image differences typically contain known features and artifacts such as residuals from bright stars, data drop-outs, and CCD frames showing saturation due to the Moon, bright planets, and proximity to the Sun.

Another artifact typically seen in the difference images, occurring to some extent in nearly every orbit, are large-scale regions in which all the cameras appear to be illuminated simultaneously, from about one up to a few minutes at a time. These regions have a very granular appearance in the difference images, and inspection of the original CCD frames reveals that the origin of this phenomenon is a random scattering of data bins with elevated values. Figure 3 shows a typical example of this phenomenon, in comparison with a normal frame and a frame containing aurora. These are readily attributed to charged-particle strikes on the CCD: the phenomenon typically appears in the polar regions, particularly when the satellite crosses the auroral zones, and during passage through the South Atlantic Anomaly. In the polar regions the particles are likely to be electrons directly entering the baffles and scattering off the optics (the CCD is not covered and there is no straight-line path from the outside to the CCD), and in the SAA the particles are likely to be protons passing through the optics chamber walls, or perhaps byproducts of collisions with atoms in the walls.

3.3. The SMEI Aurora Phenomenon

Figure 4 is an example orbit difference image in a Hammer-Aitoff projection showing, in addition to the above-mentioned artifacts, several instances of the phenomenon that we label "SMEI aurora." Here we use this term only for convenience and make no a priori claim about the physical processes these observations represent.

Like the particle-strike regions, these phenomena also occur primarily in the auroral zones and polar regions, but typically are more poleward than the particle-strike regions, which are typically seen at geographic latitudes between 45° and 75° (they could also occur concurrently with the particle strikes in the auroral zones, but in that case their presence would be masked). They are never seen in close proximity to the SAA. These phenomena show much variation from orbit to orbit, typically appearing in a single isolated orbit or are otherwise not identifiable as a consistent feature from one orbit to the next. This implies that the origin is not in interplanetary space or beyond; even CMEs passing close to the Earth are observed progressively in a sequence of orbits. The observed phenomenon is therefore occurring somewhere in the high atmosphere along the imager's line-of-sight.

The SMEI aurora is seen in two general forms. The first, here termed "flash," is superficially quite similar in appearance to the regions of intense particle strikes: bright regions in which all the cameras are illuminated simultaneously, lasting from <1 to 3 minutes or more, with a median of about 2 minutes. The distinction is that in the orbit difference images, these regions have a very smooth, not granular, appearance. The original transmitted CCD frames that compose these regions in the all-sky orbit images also show this smooth appearance, quite distinct from the effect of particle strikes.

While the majority of the occurrences of this phenomenon are as featureless on a large scale as the particle-strike regions, a significant fraction shows at least some structure, particularly along the trailing edge of the regions. Also, cases are occasionally observed in which the illumination is limited to a portion of the composite field of view, usually extending from the side cameras to some point along the middle camera. These characteristics imply that these are remotely imaged phenomena rather than instrumental background.

The illumination typically commences and ceases quite abruptly; the brighter examples in particular usually appear very sharp edged in the difference images, particularly along the leading edge. The trailing edge occasionally shows some structure. The surface brightnesses range from $\sim$1 ADU to >100 ADU, and for any given occurrence the brightness varies by less than 50% across the entire field of view. Figure 4 shows several examples of bright flash events occurring during the period of intense geomagnetic activity at the end of October 2003.

The second form, termed “streamer,” is a more peculiarly structured phenomenon. Appearing primarily in the middle (rearward-facing) camera, streamer events consist of one or more filaments curving asymptotically, with increasing time, toward the rearward direction from the satellite (approximately coincident with the center of the middle camera as shown in Figure 1b). Occurring much less frequently than flashes, streamers typically are initially observed at high latitudes, usually greater than 75°. The asymptotic line is nearly always within several degrees of the track of the satellite’s negative velocity vector. The exceptions to this behavior are streamers that are observed for prolonged periods toward very low latitudes; in these cases, the filaments can be canted or curved in any direction.

While the asymptotic streamer phenomenon is observed mainly in the middle camera, the filaments (if they are distinct enough to be traced continuously) are usually observed to originate in the side cameras where they have an appearance similar to flash events. The aurora example shown at upper left in Figure 2, a very bright streamer, is a striking example of this characteristic.

Figure 5 shows a close-up of a typical streamer event, represented in a cylindrical projection for which the instrument’s scanning motion is rectilinear from bottom to top. This representation is appropriate for displaying the middle portion of the field of view with little distortion. Also included in this figure is a reprocessed version in which the low-spatial-frequency content has been removed to reveal the structure of the filaments. Figures 2 and 4 also show examples of streamer events.

The duration of streamer events is from a few minutes to 15 minutes or more, and note that duration of an aurora event is here defined as the duration of the actual observation (as SMEI flies near it or through it) and not the underlying physical phenomenon. The brightnesses among the individual filaments in a streamer event can vary widely, from ∼1 ADU to tens of ADU or more. The filaments in a single streamer event are rarely seen to cross, and even then only toward the end of very long duration events, where streamers typically depart from the usual asymptotic behavior.

Streamer events and flash events both typically occur at high latitudes, look very similar in the side cameras, and have equivalent ranges of surface brightnesses. Also, the onset of the streamer events is very often accompanied by one or more flash events. For these reasons, flashes and streamers are likely to be related phenomena, and we thus classify them both as SMEI aurora. Streamers occur much less frequently than flash events, constituting about 20% of the total occurrence of SMEI aurora.

3.4. First-Year Survey

The orbit images for the first year of SMEI operations, from 10 February 2003 to 10 February 2004, have been surveyed for SMEI aurora activity. Approximately 70% of this total time interval contains data of sufficient quality to detect the presence of aurora.

The SMEI aurora events for this time period have been catalogued. A flash event is defined as a single episode of onset and then cessation of brightening. The distinction between aurora and enhancement due to charged particle strikes is made visually; down to about 2 ADU of excess brightness the granular appearance of particle effects is easily discerned. Streamer events are defined as a single period of time continuously occupied by streamer filaments; that is, there is no attempt to catalog individual filaments. Each SMEI aurora event is characterized by times of onset and of cessation, the corresponding geographic latitude and longitude of the satellite, the magnetic latitude and magnetic local time, the field of view center heading, and a sampled surface brightness measure. For flashes, the surface brightness is sampled at a "typical" location along its length, and for streamers, a typical point on the brightest filament is sampled. A large uncertainty results for surface brightnesses measured from difference images, so no more accurate brightness measurement is practical for the present purposes. The error in the time measurements is approximately 30 seconds, and the corresponding error in the derived geographic coordinates is a few degrees in the angular position along the orbit. More than 1000 SMEI aurora events were identified in the survey period. Table 1 summarizes the totals and mean properties.

3.5. Comparison with Geomagnetic Disturbance

Since the aurora is brightest and probably extends highest during geomagnetically active periods, one way to ascertain whether SMEI is detecting auroral light is to compare the periods of observation of the high-altitude phenomenon with known periods of geomagnetic disturbances or storms. Towards that end, we define the SMEI Aurora Measure (SAM), which we devised to provide an orbit-to-orbit accounting of the total SMEI aurora activity, and represent it as a single numerical value. For each event, the product of the duration in minutes and typical brightness is taken, and then these values are summed over the events occurring in an orbit.

We find good correlation between the peak values of the SAM and peak values of several geoactivity indices. The Kp index is a 3-hour index that has a range from 0 to 9 and is proportional to the maximum amount of fluctuation in the magnetic field. The Ap index is a linearized average of the Kp index. Figure 6a shows the SAM values and Ap indices for a geomagnetic storm occurring in mid-June 2003. Figure 6c shows how the likelihood of observing any SMEI aurora events at all in a given orbit varies with the Kp index; there is a steady increase above Kp equals 2 and a sudden jump to >80% at Kp equals 6.5. Figure 6b shows the SAM plotted vs. Kp (dots) for all the orbits where data were available. At any given Kp level there is a large scatter of SAM values, but these results suggest that at a given SAM value, there is an approximate lower limit to the Kp level, indicated by the solid line. This is an expected behavior if the phenomenon SMEI is observing is intermittent and is episodically sampled by the polar passages. The crosses indicate the mean SAM value in each Kp bin. The mean SAM values correlate well with the Kp levels in the aggregate, and once again there is a discontinuity in the relation at about Kp equals 6.

The Dst index is commonly used by researchers as a physics-based measure of the general level of geoactivity. The hourly Dst index is provided by the World Data Center in Kyoto, Japan (http://swdcdb.kugi.kyoto-u.ac.jp/dstdir/). Dst is a global measure of the Earth's current ring, which becomes energized during geomagnetic storms: a strong current drives the horizontal magnetic field to increasingly negative values. Generally, a level of hourly Dst below -50 nT is considered to define a moderate-level storm. To be conservative, we defined and recorded as storms all periods of Dst < -60 nT from March through October 2003. The Dst values available for this time period are labeled "provisional"; i.e., most important corrections have been applied, but the values are not yet definitive. We found 34 periods greater than 1 hour duration for which Dst < -60 nT and SMEI also produced good data. During 88% (30 of 34) of these intervals, SMEI observed some aurora activity (non-zero SAM values). SMEI aurora activity is observed in about 20% of orbits overall. Eight of the 30 periods were during major storms (Dst $<$

-100 nT). Thus, there is a very good association between the SAM index and geomagnetic storms.

We can ask how closely the peak values of the SAM and Dst match by comparing these measures in the other direction, peak SAM to Dst. We found 43 periods of either single or two or more contiguous orbits during which the SAM was nonzero and reached > 50 ADU minutes in some orbit. We found that 63% (27 of 43) of the periods contained peak Dst < -60 nT. If we eliminate the periods consisting of a single orbit, the association rises to 72% (21 of 29).

3.6. Persistence

The good visual coverage of the polar caps in each orbit, and the 102-minute cadence of the polar cap passages, suggests that it should be possible to investigate the persistence of these aurora phenomena with the SMEI data set. The streamer event shown in Figure 5, for example, was preceded in the previous orbit by another streamer event, shown in Figure 7, with a very similar appearance at the same relative position in the orbit. Streamer events are not seen in the earlier or later orbits, implying that the phenomenon has a lifetime of greater than 100 but less than 200 minutes. However, in this case, while the general arrangement of filaments is very similar in both events, there is no obvious way to identify and match individual filaments between the two events; the filaments are not distinctive enough, and the westerly rotation of the ground track from orbit to orbit presumably changes the perspective sufficiently to prevent reliable correspondence in any case. We therefore cannot determine if these two streamer events represent the same structures, or if we are seeing separate short-lived phenomena that happen to occur ∼100 minutes apart.

Flash events also show occasional similarities from orbit to orbit. The bright flashes at the upper left in Figure 4, for example, are separated by deep shadows, which indicate the presence of flash events at nearly the same locations in the previous orbit. Note that Figure 4 is a running difference image. The featureless nature of the flashes makes determining correspondence especially problematic. A detailed model of the flashes and streamers will be necessary before the persistence of the aurora events can be studied.

4. Discussion

The SMEI orbit is at 840 km, and the cameras are aimed obliquely upward, so the observed phenomenon is at or just above the satellite's altitude, if a local phenomenon, and possibly much higher, if viewed from some distance. The very high altitude sunlit auroral rays reported by *Størmer* [1955], observed at heights of 700–1100 km, did not extend, as a visible phenomenon, below the shadow line; occasionally a ray that faded down into the shadow reappeared at much lower altitudes. It is worth noting that SMEI is nearly always in sunlight, except for brief periods at the southern extreme of its orbit for a few weeks around midsummer, and its field of view is likewise nearly always in sunlight.

The visible emission of the high altitude aurora has been attributed to resonant scattering of sunlight by the N_2^+ ion (*Hunten* [2003] and references therein). *Romick et al.* [1999], using the spectrographic imagers on the MSX satellite, made the first optical detection of N_2^+ at high altitudes, observing spectral features up to ~900 km over the northern polar cap during a period of modestly elevated geomagnetic activity (Kp equals 3). Observations a day later, at Kp = 1, yielded no observed features above ~600 km.

Romick et al. [1999] analyzed the brightest set of N_2^+ optical spectral features, vibrational transitions known as the 1st Negative bands. The strongest of these bands lie between 300 and 475 nm and are therefore below the effective short-wavelength limit of the SMEI passband, although the set of features at 450–475 nm is detected at about 20% peak responsivity. Another set of vibrational transitions, the Meinel bands, are well represented within the SMEI passband, but these are generally weaker lines than the 1st Negative bands [*Broadfoot*, 1967; *Degen*, 1981], due to a reduced solar excitation probability, and the spectroscopy of *Romick et al.* [1999] qualitatively confirms this expectation. For the 1st Negative bands from 380 to 395 nm, they find a total integrated intensity, for the Kp equals 3 observations, of 1–1.5 kR (1 Rayleigh = $10^{10}/4\pi$ photons $\mathrm{m}^{-2}\mathrm{s}^{-1}\mathrm{sr}^{-1}$) at the highest altitudes, 800–900 km. The Meinel bands measured over the SMEI passband are predicted to have a total brightness ∼2 times lower than this [*Degen*, 1981], and so with SMEI we would expect to observe 500–750 R under analogous conditions, with the broad assumption of a similar viewing geometry.

With the conversion 1 ADU = 36 R, described in Appendix A, a SMEI brightness of ∼15–20 ADU is estimated for the event observed by *Romick et al.* [1999] In the survey of SMEI aurora observations, 47 flash events were observed at Kp equals 3. The median surface brightness for these events was 3 ADU, but the values ranged from the effective threshold at 1 ADU up to 36 ADU. The predicted SMEI brightness for the observation of *Romick et al.* [1999] does fall well within the range of observed SMEI aurora events, though it is a factor of ∼4–5 higher than typical for this Kp level. At Kp equals 1, at which no N_2^+ emission was detected with MSX above 600 km, only 11 SMEI flash events were observed, with a maximum brightness of 6 ADU.

It should be noted that with this ADU-to-Rayleigh conversion, SMEI may be sensitive enough that the resonant scattering mechanism may not be required to explain the detections in all cases; *Romick et al.* [1999] also observe the OI multiplet at 630.0 nm at an intensity possibly sufficient to explain by itself the brightness, at a few ADU, of the fainter SMEI observations.

The presence of N_2^+ at high altitudes has been generally attributed to ion upflow during periods of elevated geomagnetic activity. Experiments using in situ ion mass spectrometers [*Hoffman et al.*, 1974; *Craven et al.*, 1985; *Yau et al.*, 1993] have detected N_2^+ ions at altitudes $>$ 1000 km and with densities consistent with the *Romick et al.* [1999] observations. If we can regard the SMEI aurora detections as a tracer of high-altitude molecular ions, then the regular coverage and sampling of the polar cap regions these observations offer could make the SMEI data set a useful tool in studying the morphology of the molecular ion upflow phenomenon. Towards that end, we attempt a preliminary interpretation of the physical structures represented by the SMEI observations:

4.1. Flashes

As previously noted, if these phenomena are not local then their origin must be literally filling the sky observed by SMEI. The results of *Yau et al.* [1993] and *Taylor* [1974] suggest that molecular upflow can be an extremely localized phenomenon, with upflow region sizes ranging from as low as 100 km up to ∼1000 km in lateral extent. With an assumption of local origin, the flashes are most easily explained as transits of the satellite through a luminous medium. This provides an explanation for both the uniform brightness across the field of view, and the abrupt commencement and cessation of the illumination .

With this interpretation, the duration is a measure of the lateral extent; the range of durations, and the ∼7 km/s orbital speed, suggest sizes from 200 km to 1500 km with a median of about 700 km, in approximate agreement with the *Yau et al.* [1993] results.

This is somewhat higher than the 500 km upper limit inferred from the narrow latitude distribution at the northern and southern limits of the orbit, but not problematically so as the errors in the time determination for the boundaries of the events can yield size errors of a few hundred kilometers.

One consequence of this interpretation is that the luminous regions responsible for most flash phenomena must not extend more than a few hundred kilometers above the height of the satellite. The reason is that a high region would continue to be observed, after the satellite exited, in the rearward field of view as a centralized peak (i.e. at least a short, wide central streamer). A region 700 km in lateral extent, which we may take as typical for a flash-producing region, would fill the 60° width of the middle camera from a distance of 600 km from the region's center ($\sim$30 seconds after the satellite exited), and occupy about half the camera's field of view at 1300 km. If the region remained visible at much greater than 600 km, it would cause a noticeable extension of the flash event along the trailing edge over a limited lateral extent. For structureless flash events, the vast majority, the upper visible limit of the transited region must be below the field of view before the satellite is far enough away to observe the region only in the middle camera; with the 30° elevation of the cameras this becomes a limit of $\sim$350 km above the satellite's altitude. Interestingly, this gives a limit to the visible height about equal to the altitude limits for the high sunlit aurora observed by *Størmer* [1955].

With this explanation of flash events it would be expected that at least some fraction of transited regions would extend high enough to be visible in the cameras long after the satellite has exited. While many flash events do show some minor unevenness along the trailing edge, concrete structure is not common. Figure 8 demonstrates a few examples.

Figure 8a shows a short, diffuse extension that subtends about half the middle camera, slightly left of center. Figure 8b shows broad, diffuse material extending the width of the middle camera. Figures 8c and 8d show more localized trailing peaks.

That unambiguous structure is never observed along the leading edge of a flash event is strong evidence in favor of this picture of the origin of flash events. The brightness profile at the leading edge of a flash event is strictly a matter of increasing line-of-sight path length through the transited medium, and so the cameras should never see anything other than uniformly increasing illumination. For a region of limited height above the satellite, the brightness should increase rapidly to some maximum. Structure should only appear after the satellite has exited the region, when the region can be observed at some distance from the rearward-looking and upward-angled cameras.

The brightness discrepancy between the observations of *Romick et al.* [1999] and the SMEI flash events at a similar Kp value could possibly be explained as a path length difference. If SMEI observes a flash event due to a transit through a height-limited region, it is looking through perhaps at most a few hundred kilometers of material, from the satellite's altitude to the height limit at an oblique angle. The MSX observations, slightly down-looking through the atmosphere, were most likely observing the entire thickness of the region from some distance away. If the region were at the larger end of the range suggested by the flash observations, > 700 km, then a factor of two or more between the observed brightesses can be justified.

If flash events represent transits, the location of the satellite during an aurora observation represents the location of the aurora phenomenon itself. Figure 9 shows the locations of the flash events converted to magnetic local time (MLT) and magnetic latitude (MLAT), for both the northern and southern hemispheres. In the north, there are clear clusterings of flash events in the region 1000–1200 MLT and 73°-76° MLAT, which corresponds approximately to the cusp region, and within a few degrees of the magnetic pole in the early afternoon period.

This clustering should be taken with some amount of skepticism, as the satellite track crosses both the magnetic pole and the cusp region near the (geographic) northernmost extent of the orbit, and we therefore expect an increase in the density of observations at those points simply from the geometry of the orbit track coverage, and noting that the northernmost point in the orbit occurs near noon MLT. The increased density of observations at the pole and cusp should, however, only be about 10% greater than the intervening magnetic latitudes for a random distribution of observations in the orbit. The observed clustering is much greater. That the centers of the clusters, at about 1100 MLT and 0100 MLT, occur distinctly away from noon also indicates that this clustering is a real effect. Also, in the north, observations at low MLAT ($< 70°$), occurs almost exclusively in the dusk region.

In the south, there is no clustering of observations, but this is likely to be an orbit-coverage effect. The satellite track, usually on the nightside at the southernmost point, crosses the cusp region only for a brief period around the winter solstice, and the magnetic pole crossings are also usually nightsided. As in the north, the low (less negative) latitude observations are primarily in the dusk region, with a moderate emphasis on the nightside but this is also most likely a sampling effect.

Finally, we consider the question of ram or shuttle glow as a possible origin of or contributor to the flash events. Shuttle glow is generally observed along surfaces of satellites facing in the ram direction, with the spectrum peaking at about 700 nm (close to the peak of SMEI responsivity), and has been attributed to the combination of atmospheric O and NO to NO_2^* [*Murad*, 1998]. The phenomenon is highly altitude (i.e. density) dependent. While the 840 km altitude of the SMEI orbit and the fact that the cameras are rearward-facing suggest that shuttle glow should not be a significant effect in the images, the high sensitivity of the SMEI cameras must be considered. *Torr et al.* [1977] observed what was later termed shuttle glow as a contamination of airglow measurements with the Atmospheric Explorer C satellite. While the contamination was strongest at low altitudes ($<$ 170 km) and in the ram direction, they also observed contamination to a level (at 730 nm) of a few tens of Rayleighs at the highest altitudes ($\sim$500 km) and in the wake direction. This is equivalent in brightness to the faintest end of the flash events. If we postulate an enhanced population of neutral species as well as ions in the regions causing the flash events, we cannot rule out a priori this phenomenon as a contributor.

Shuttle glow could explain the abrupt commencement and cessation of the flash events, if we presume passage of the satellite through a localized region of elevated density. It remains a question, however, whether shuttle glow could produce a uniform illumination of the field of view, and if so, it would require an unvaryingly uniform appearance of the flashes. That we occasionally observe definite trailing-edge structure in the flash events, and also partial flash events, rules out the possibility that shuttle glow is the sole cause of the flash events, but it could be a contributor.

4.2. Streamers

The primary characteristic of the streamer events is that the component filaments in the orbit difference images curve asymptotically toward the rearward viewing direction with increasing time. This is most straightforwardly interpreted as a perspective effect: objects initially observed nearby are observed toward increasingly rearward directions as the satellite progresses around its orbit. As objects that are observed at increasing distances are also observed at increasing heights (Figure 1c), this implies that the streamer filaments represent columns of luminous material. The filaments in Figure 5 (also Figure 6) are observed for about 10 minutes following the initial observation; the geometry suggests that the observed height at the end of the streamer event is > 2000 km above the altitude of the satellite.

The trailing-edge features of the flash examples in Figure 8, particularly 8c and 8d, have the general appearance of streamers. This suggests a continuum of geometric phenomena responsible for both: low-altitude luminous regions or columns are visible to the upward-looking cameras only when the satellite transits the region, and result in uniform illumination of the field of view. Higher altitude columns yield some visible structure along the trailing edge after the satellite has exited. Much higher columns are visible from greater distances, with or without a prior transit.

This picture can explain the common characteristic of the streamer filaments that they originate at the far ends of the side cameras, as shown in Figure 2. If SMEI observes a high column from some transverse distance, it will always be first observed at one extreme edge of the field of view, because the field of view is directed rearward. The viewing direction to the column then sweeps toward the rear as the satellite progresses along the orbit, rapidly crossing the side camera to the middle camera. This motion occurs over a brief period, giving the appearance of a flash toward the sides in the orbit image.

A column more distant from the satellite path will progress to the rearward direction at a slower rate. A few examples have been observed of streamer filaments that show the characteristic asymptotic behavior in the side cameras, curving gradually toward the rearward track, but usually terminating before reaching the middle camera.

With this interpretation of the streamer events, the curvature and width of well-defined streamer filaments can in principle be transformed into estimates of their position on the Earth, relative to the satellite, and their physical diameter and visible heights.

Figure 10 shows the results of simulating and fitting streamer filaments with a simple geometric model. For the model, the filament observations are assumed to represent luminous columns of circular cross section extending radially outward from the Earth. The parameters are the geographic longitude and latitude of the column, the radius, and the height. In the simulation, the orbital position and the attitude of the satellite are evolved through the relevant time interval, and at each time step the contours of the column are mapped onto the focal plane and thence projected onto the corresponding orbit image. The objective is to match the contours of the observed filament, and the parameters are, for the current purposes, optimized by hand.

Assuming the model is reasonably representative of the actual structures, the parameters can be determined with reasonable precision without a formal fitting procedure because each can be optimized independently: the curvature of the model filaments in the simulation is established solely by the satellite's distance of closest approach, and their position in the orbit image is established by the relative position along the orbit path. The radius and height are likewise determined independently. For the two examples in Figure 10, the original images are shown, along with the fitted column contours and the resulting sizes and locations on the Earth relative to the orbit ground track. For these cases, the filament contours can be matched quite well with the model; the positional tolerance is less than ∼1°. The resulting model parameters suggest that the filaments in these cases represent columns 30–100 km in diameter whose visibility extends to ∼2000 km altitude.

The model is of course too simple to yield any generally reliable quantitative results. The examples in Figure 10 have been selected for a specific property the model requires for a good fit, that the filaments converge exactly on the rear-facing track in the images. That the model closely reproduces the configuration of the filaments is, however, strong evidence that this picture of the origin of the streamer events is basically correct. Figure 11 shows an example for which the observed streamer filaments converge several degrees away from the rearward track, and it is obvious that the model fit contours do not match the filaments. But even in this case the shapes of the projected model columns conform in basic morphology to the observed filaments, and clearly some generalization of the model to allow canting or curvature of the columns, to reflect the anticipation that these structures will likely follow magnetic field lines, would permit a more accurate fit. Also, in this case, while the model height of the filaments, >10000 km, is itself not literally realistic, it does suggest that these objects are being observed to some extreme altitude.

The interpretation of the streamer filaments is that they represent typically narrow (∼100 km) columns of material extending from the satellite's altitude up to perhaps 2000 km or more. In situ measurements of molecular ion upflow also typically show very confined regions at least in latitude (longitude extent being a more problematic determination in these experiments). *Taylor* [1974], using the ion mass spectrometer on the OGO-6 satellite, found $\sim 10^3$ enhancements of molecular ion density, over a quiescent value of a few per cm^3, at 1000 km altitude over very narrow, 2°–3° latitude zones at high latitude (MLAT $> 65°$) during periods of modestly elevated geomagnetic activity (Kp equals 4–5). Molecular ion enhancements of $\sim 10^2$ were also seen at Kp equals 2, again in very localized regions. For comparison, the flash events in SMEI are observed down to Kp equals 1, and the streamer events first appear at about Kp equals 3.

Yau et al. [1993], using the mass spectrometer on the Akebono satellite, observed regions of upflowing N_2^+ ions at very high altitudes, ∼6000 km. These regions were also very localized in latitude, as narrow as 1°-2°, observed over high magnetic latitudes (75° - 85°), and were primarily dayside events. The SMEI streamer events are also primarily dayside (in contrast to the flashes, which are about evenly divided between dayside and nightside), and are also observed at high latitudes and at least somewhat elevated Kp levels. Molecular upflow was observed in about 3% of the examined polar passes of the Akebono satellite; streamer events are observed in about 5% of SMEI orbits.

Yau et al. [1993] assume a cusp/cleft origin for molecular upflow, and infer from the very high latitude detections that molecular upflow regions convect poleward toward much greater heights. The overall distribution of location for the onset of SMEI streamer events in MLT and MLAT follows that for the flashes (as in Figure 9) but with a much smaller percentage of nightside observations. While many streamer events do seem to originate in the cleft/cusp region, the distribution of streamer event observations suggests also that the very high latitude molecular upflow regions could originate from the polar cap. One caveat of this interpretation is that the location of the satellite is not necessarily a good indicator of the location of a SMEI streamer filament object; the actual filament could be

5° or more from the location of the satellite at the initial observation. An accurate model for the streamer filaments would be necessary to conclude a cusp or cap (or otherwise) origin for a given streamer event.

For example, many of the filaments in the streamer events shown in Figure 5 and Figure 6 have a curvature that indicates a source close to the orbit track (as indicated by the column model for the filaments). The onset of these events occurs when the satellite is within about 5° of the magnetic pole (at 113W, +82) and so the filaments also are likely to originate near the pole. The column-model fitting result for the northern hemisphere example shown in Figure 10, likewise, indicates that the filaments originate within 10° of the magnetic pole. These are both likely to be polar cap events.

The high altitude of the *Yau et al.* [1993] observations suggest we should also consider the highest altitude SMEI streamer observations, which we may identify as those with the longest duration. These are typically observed through the auroral zone and beyond to lower latitudes, keeping in mind that SMEI is looking back approximately toward the pole as it descends toward the equator. Thirteen streamer events in the survey were observed to lower than 45° magnetic latitude; the median Kp index was 7 for these events.

Figure 12 shows a representative example, from 27 July 2003; Kp equals 5 during this period, and reached 6 in the preceding 6 hours. In this event, actually a series of events, a typical streamer is first seen when the satellite is at about +80° geographic latitude, ∼15° poleward of the auroral zone; the filaments for this streamer event, with an initial brightness of ∼30 ADU, are observed for about 10 minutes well into the auroral zone. Four minutes later, at +70° latitude, is a very bright flash, ∼90 ADU, and immediately following this, approximately at the poleward boundary of the auroral zone, is the onset of the long streamer filaments. These are observed for about 15 minutes, down to about +20° latitude.

These streamer filaments are much fainter than the earlier events, a few ADU at the brightest. Typical for long filaments observed below the auroral zone, they do not converge on the rearward track but instead have somewhat irregular behavior. The filament to right of center in the image curves to the right. The line-of-sight to the magnetic pole at this time is about 15° to the left of center, so this curvature is approximately equatorward. The filament on the left curves in the opposite direction; this is also generally away from the pole. That we see these filaments at all down to these low latitudes, and that they have only slightly diminishing apparent diameters, suggests that all these filaments are curving equatorward along the line-of-sight, toward the satellite. It is difficult to interpret these filaments as trending poleward.

The initial streamer in this example, itself a long duration event, is first observed when the satellite is at 1100 MLT and 73° MLAT. The IMF B_z is within ±5 nT during this period and so the satellite is likely to be within or near the cusp at this time [*Newell et al.* 1989; *Frey et al.* 2003]. The column model indicates a position for the filaments about 3°-4° from the ground track, and a few degrees farther back along the orbit track, and so the filaments originate approximately from the poleward side of the cusp. The filaments for this event converge very close to the rearward track, and at this point line-of-sight to the magnetic pole is far to the left in the image, so for this case also a poleward trending is not indicated, although the behavior at much higher altitudes cannot be ascertained. A cusp origin for this event also indicates, however, that the long low-latitude streamer event occurring later originates deep into the auroral zone. This could explain the evident equatorward curvature, if we presume that the filaments will follow closed magnetic field lines.

We thus observe long-duration streamer events likely to be originating in the cap, the cusp/cleft, and the auroral zone. If the streamer filaments do in fact represent columns of upflowing molecular ions, this indicates that the picture of cleft-originated molecular ions convecting poleward suggested by *Yau et al.* [1993] is not necessarily correct; molecular ions can originate at all magnetic latitudes from the auroral zone up to the pole.

5. Summary and Conclusions

The SMEI instrument on the Coriolis satellite makes 14 passes per day through both the north and south polar caps at an altitude of 840 km. In each orbit nearly 4π steradians of the sky is imaged, for the purpose of detecting and tracking faint heliospheric disturbances out to 1 A.U. and beyond. Over the ~3600 orbits with good data for the first year of normal operations, from 10 February 2003 to 10 February 2004, 680 orbits contained evidence of a visual phenomenon occurring at or above the height of the satellite, whose morphology and orbit-to-orbit variation indicates an atmospheric origin, and which occur almost exclusively from the auroral zones to the magnetic poles. About 1000 individual events have been recorded. The occurrence, frequency, and brightness of the events are well correlated with enhanced geomagnetic activity as measured by the Kp and Dst indices, and for this reason we term the phenomenon “SMEI aurora.”

The SMEI aurora appears in two basic forms. The first is the simultaneous uniform illumination of all three cameras, which have a total instantaneous field of view of approximately $3^\circ \times 150^\circ$. An interpretation of these “flash” events is that they represent passage of the satellite through a luminous medium from one to several hundred kilometers in lateral extent. The second is a more localized phenomenon in the all-sky orbit images, consisting of one or more filaments that curve asymptotically, with increasing time, toward the rearward direction from the satellite. A tentative interpretation of these "streamer" observations, about 20% of the total SMEI aurora, is that they represent localized columns of luminous material occasionally extending to possibly great heights ($>$ 2000 km) above the satellite's altitude. The height of these columns suggests that they should be easy for SMEI to observe, as they can be seen from a distance, but their relative infrequency suggests that they are much rarer phenomena than the flash-causing structures.

In the northern hemisphere, about 40% of the total events occur either in the cleft/cusp region or toward the magnetic pole in the early afternoon in MLT. The balance are distributed from the northern limit of the auroral zone across the cap, and to lower magnetic latitudes in the dusk region. On the dayside, the distribution of flash and streamer events is similar, but very few streamer events are observed on the nightside.

The orientation of the orbit causes the southern polar passages to be primarily night-sided, and so the sampling is insufficient to compare the distribution with the dayside clustering seen in the north. Apart from the resulting gap at high magnetic latitudes on the dayside, the southern events are distributed fairly evenly from the auroral zone poleward, and the low-latitude duskside distribution is also seen.

The regions responsible for most flash phenomena are likely to be limited in visible height to a few hundred kilometers above the altitude of the satellite, as indicated by the typical lack of definite structure at the trailing edge. The median size, as suggested by the flash durations, is about 700 km. This is much larger than the diameters suggested by the column model for the streamer filaments, $\sim$100 km or less, at least for a small number of cases analyzed, but these seem to be typical. These results suggest that the flash-causing regions and those represented by the streamer filaments are distinct populations. This could explain why there are few cases observed of prominent central streamer filaments following a flash event: it would be a rare occurrence for the satellite to pass directly through or underneath these narrow objects. A related possibility is that the streamer filaments are narrow high-altitude extensions of broader lower-altitude regions that occur under some set of conditions. This is supported by the fact that the onset of streamers and flash events very often occur in close proximity.

SMEI is a broad-band instrument and so we have no direct information about the specific emission or excitation processes responsible for the observations. The visibility of aurora at heights $\geq$800 km, occurring during magnetic storms, is generally attributed to resonant scattering of sunlight by N_2^+ ions. With a preliminary calibration of the SMEI instrument, the surface brightness of the SMEI aurora events is consistent with this mechanism, but SMEI may also be sensitive enough that this specific emission mechanism may not be required to explain many of the observations. As excitation of the 630.0 nm oxygen line does not require sunlight [*Henriksen et al.*, 1984], and it is optically detectable at low levels, at the SMEI altitude or higher, during geomagnetic disturbances [*Romick et al.*, 1999], one question to investigate is whether SMEI observes any aurora events while the satellite is in shadow. Unfortunately, these periods are very brief, limited to a few minutes at the southern extremity of the orbit for a few weeks around midsummer, and the aurora or enhanced geomagnetic activity may not have occurred at these times. Therefore, we cannot speculate on this possibility.

Molecular ion upflow during periods of geomagnetic activity is generally assumed to be the process leading to very high altitude aurora. If the SMEI cameras are indeed recording emission from upflowing N_2^+ ions, then the regular passage through the polar cap regions, and the high degree of coverage above ~1500 km, may make the SMEI data set a useful tool for studying the morphology of this phenomenon.

Appendix A: Calibration

The various corrections applied to the values in the raw CCD frames are assigned such that an exposure to a uniform illumination will result in a uniform response in the data values. This means that the response will be proportional to the radiance of a source over the SMEI passband. If we let R_λ represent the photon flux responsivity of the SMEI detectors (Figure 13), then the energy flux responsivity is proportional to λR_λ. For the fully corrected data values, the response in ADUs, denoted S_{ADU}, can be expressed

$$S_{ADU} \propto \int I_\lambda^C (\lambda R_\lambda) d\lambda \tag{A1}$$

where, for notational simplicity, the superscript C on the intensity I_λ represents the convolution of the sky intensity with the system point response function (PRF). Since the ADU brightness scale is used consistently from the corrected CCD frames to the final orbit images, this expression will hold for all image representations, assuming a proper PRF convolution function is applied.

This relation can be expressed

$$S_{ADU} = \alpha \int \frac{I_\lambda^C R_\lambda d\lambda}{\frac{hc}{\lambda}} \tag{A2}$$

The integrand represents photons $\mathrm{s}^{-1}\mathrm{m}^{-2}\mathrm{sr}^{-1}\mathrm{nm}^{-1}$ (and noting that R_λ is peak normalized to 1). One Rayleigh $= 10^{10}/4\pi$ photons $\mathrm{s}^{-1}\mathrm{m}^{-2}\mathrm{sr}^{-1}$ and so we can define a broad-band brightness in Rayleighs as

$$S_{Rayleighs} = \frac{4\pi}{10^{10}} \int \frac{I_\lambda^C R_\lambda d\lambda}{\frac{hc}{\lambda}} \tag{A3}$$

and thus

$$\frac{S_{Rayleighs}}{S_{ADU}} = \frac{4\pi}{\alpha 10^{10}} \tag{A4}$$

Calibration is a question of determining the value of α. For a point source, we can integrate Equation A2 over the solid angle subtending the source,

$$\int S_{ADU} d\Omega = \alpha \int\int \frac{I_\lambda^C R_\lambda d\lambda}{\frac{hc}{\lambda}} d\Omega \tag{A5}$$

Assuming backgrounds can be removed, and the source is sufficiently isolated, then on the right hand side, the integration of I_λ over solid angle yields the source flux F_λ, and on the left hand side, the integration is the SMEI source irradiance in ADU steradians. Substituting and solving for α yields

$$\alpha = \frac{\int S_{ADU} d\Omega}{\int \frac{F_\lambda R_\lambda d\lambda}{\frac{hc}{\lambda}}} \tag{A6}$$

The SMEI irradiance was measured from orbit images. For the source flux F_λ, we used the Pickles stellar spectral templates [*Pickles*, 1998]. The calibration stars were selected to meet several criteria, using information obtained from the SIMBAD database: 1) Brighter than 4th magnitude in the V band; 2) Either non-variable or with a brightness variation less than 5%; 3) Any companion(s) must be at least 4 magnitudes fainter; and 4) The corresponding spectral template must be available.

Forty-eight stars were selected to meet the criteria. For each star, the B and V magnitudes were converted into fluxes, applying the zero-magnitude fluxes of *Bessel* [1990]. The spectral template for the star was then integrated over the Johnson V band spectral response, and the template was then scaled to match the V band magnitude, giving an estimated F_λ for the star. The template-derived B band flux was calculated from F_λ and compared to the measured B flux; a deviation of 10% or more was an additional criterion for omitting a star. Ten of the 48 stars were deleted for failing this criterion.

To measure the SMEI star irradiances, 26 orbit images were selected over the first year's data. For this purpose, the higher-resolution intermediate form of the orbit images were used, with $12' \times 12'$ pixels. For each star on each orbit image, the star was visually inspected for data quality, and rejected if unsuitable (usually either missing from the image entirely or contaminated by particle strikes). For each accepted star, the star image was extracted on a $2^\circ \times 2^\circ$ grid, a background was removed, and the brightness in ADU was summed over the pixels. The irradiance in ADU steradians was determined by multiplying this sum by the pixel solid angle. The star's measured irradiance values were averaged over all the orbit images on which it appears. Each star was measured on 10 to 20 of the 26 orbit images.

Table 2 shows the results for each star. Of the 38 stars measured, one was rejected for very high variance in the set of irradiances over the orbit images, and two were omitted for being 5σ outliers.

For individual stars, the RMS scatter in star irradiance values over the orbit images ranged from 2 to 4%, but each star presumably had some systematic error due to imperfect removal of backgrounds. We expect, however, that this error is approximately random from star to star. Other sources of star-to-star random error are the scaling factor for the spectral template (through the V magnitude) and the fidelity of the template to a star's true spectrum. There has been no attempt to correct for interstellar reddening, and this could introduce a small systematic error, but we can check this by considering bright main sequence stars, which should be the least affected. The seven main sequence stars in the calibration set brighter than V∼2 have a mean derived ADU-to-Rayleigh conversion equal to the global mean, with a small variance, indicating that reddening is not an important factor in the results.

Thus regarding the scatter of ADU-to-Rayleigh conversion results as random distribution, we have

$$1ADU = 36(\pm 1)Rayleighs \tag{A7}$$

where Rayleighs are defined in a broad-band sense through Equation A3.

Acknowledgments. SMEI was designed and constructed by a team of scientists and engineers from the U. S. Air Force Research Laboratory, the University of California at San Diego, Boston College, Boston University, and the University of Birmingham, in the U.K. Financial support was provided by the Air Force, the University of Birmingham, and NASA. For the Dst values, we thank the WDC for Geomagnetism, Kyoto Dst index service, Dst stations and the persons who derive the index. For the Kp index we thank the individuals at the Institut für Geophysik at Göttingen University who derive the index, and NOAA who make it available on their website. Lastly we thank the staff of SIMBAD and the Centre de Données Astronomiques de Strasbourg.

References

Akasofu, S. I., Aurora, in *From the Sun*, edited by S. T. Seuss and B. T. Tsurutani, AGU monograph, p. 1, 1998

Bessel, M. S., UVBRI Passbands, *Pub. Astron. Soc. Pac. 102*, 1181, 1990

Broadfoot, A. L., Resonance scattering by N_2^+, *Planet. Space Sci., 15*, 1801, 1967

Calabretta, M. R., E. W. Greisen, Representations of celestial coordinates in FITS, *Astron. and Astrophys., 395*, 1077, 2002

Craven, P., R. C. Olsen, C. R. Chappell and L. Kakan, Observations of molecular ions in the Earth's magnetosphere, *J. Geophys. Res., 90*, 7599, 1985.

Degen, V., Vibrational enhancement and the excitation of N_2^+ and the first negative system in the high-altitude red aurora and the dayside cusp, *J. Geophys. Res., 86*, 11,372, 1981.

Eyles, C. J., G. M. Simnett, M. P. Cooke, B. V. Jackson, A. Buffington, N. R. Waltham, J. M. King, P. A. Anderson, and P. E. Holladay, The Solar Mass Ejection Imager (SMEI), *Solar Physics, 217*, 319, 2003

Frey, H. U., S. B. Mente, S. A. Fuselier, T.J. Immel, and N. Østgaard, Photon aurora in the cusp during southward IMF, *J. Geophys. Res., 108(A7)*, 1277, doi10.1029/2003JA009861, 2003

Henriksen, K., C. S. Deehr, G. J. Romick, G. G. Sivgee, N. I. Federova and G. F. Totunova, Low energy enhancement of the OI 630 nm line and enhancement due to resonance excitation of the N_2^+ first negative bands, *Annales Geophysicae, 2*, 191, 1984

Hoffman, J. H., W. H. Dobson, C. R. Lippincott and H. D. Hammack, Initial ion composition results from the ISIS-2 satellite, *J. Geophys. Res., 79*, 4246, 1974

Hunten, D. M., Sunlit aurora and the N_2^+ ion: a personal perspective, *Planet. Space Sci., 51*, 887, 2003

Jackson, B. V., D. F. Webb, R. C. Altrock and R. Gold, Considerations of a Solar Mass Ejection Imager in a Low Earth Orbit, in *Eruptive Solar Flares*, edited by Z. Svestka, B. V. Jackson and M. E. Machado, p. 322, Springer-Verlag, New York, 1992

Jackson, B. V., A. Buffington, P. P. Hick, S. W. Kahler, E. Cliver, S. Price, J. Johnston. P. Anderson, P. Holladay, D. Sinclair, T. Kuchar, D. Mizuno, S. L. Keil, R. Radick, J. Mozer, R. C. Altrock, R. Gold, G. M. Simnett, C. J. Eyles, M. P. Cooke, N. R. Waltham and D. F. Webb, The Solar Mass Ejection Imager (SMEI): The Mission, *Solar Physics*, 2004, in press.

Murad, E., The shuttle glow phenomenon, *Ann. Rev. Phys. Chem., 49*, 73, 1998

Newell, P. T., C.-I. Meng, D. G. Siebeck, and R. Lepping, Some low-altitude cusp dependencies on the interplanetary magnetic field, *J. Geophys. Res., 94*, 8921, 1989

Pickles, A. J., A Stellar Spectral Flux Library: 1150–25000 Å, *Astrophys. J., 110*, 863, 1998

Romick, G. J., M. F. Morgan, D. Morrison, L. J. Paxton, C.-I. Meng, Polar cap optical observations of topside (>900 km) molecular nitrogen ions, *Geophys. Res. Lett., 26*, 1003, 1999

Størmer, C., 1955. The Polar Aurora. Clarendon Press, Oxford.

Tappin, S. J., A. Buffington, M. P. Cooke, C. J. Eyles, P. P. Hick, P. E. Holladay, B. V. Jackson, J. C. Johnston, T. Kuchar, D. Mizuno, J. B. Mozer, S. Price, R.

R. Radick, G. M. Simnett, D. Sinclair, N. R. Waltham, and D. F. Webb, Tracking a major interplanetary disturbance with SMEI, *Geophys. Res. Lett., 31*, L0282, doi:10.1029/2003GL018766, 2003

Taylor, H. A. Jr., High latitude ion enhancements: a clue for studies of magnetosphere-atmosphere coupling, *J. Atmos. Terr. Phys., 36*, 1815, 1974

Torr, M. R., P. B. Hays, B. C. Kennedy, J. C. G. Walker, Intercalibration of airglow observatories with the atmosphere explorer satellite, *Planet. Space Sci., 25*, 173, 1977

Yau, A. W., B. A. Whalen, C. Goodenough, E. Sagawa and T. Mukai, EXOS D (Akebono) observations of molecular NO^+ and N_2^+ upflowing ions in the high-altitude auroral ionosphere, *J. Geophys. Res., 98*, 11,205, 1993.

Figure 1. The geometry of the SMEI observations of the topside ionosphere. a) Schematic of the Coriolis satellite in orbit, showing how the SMEI cameras are mounted and the orientation of the fields of view. b) Schematic of the rearward-facing hemisphere (opposite to the velocity vector) as seen from the satellite. Shown are the fields of view of the three cameras on the sky and the location of the Earth. The satellite orbit, nearly circular at an altitude of 840 km, follows approximately the terminator line. c) Schematic showing how the field of view of the SMEI cameras, over a given point over the Earth's surface, samples an increasing altitude with time. d) The sampling of the topside ionosphere for a single orbit track (solid line) crossing the northern polar cap. The dotted lines delineate the region sampled down to 1000 km (or lower) and the dashed lines delineate the region sampled down to 1500 km. About half the polar cap $> 60°$ is sampled from 1500 km and up during each orbit.

Figure 2. Example of an all-sky orbit image in a sun-centered Hammer-Aitoff projection, from 30 May 2003, 0400-0541 UT. Ecliptic coordinates are displayed at upper right. The position of the Sun is indicated with a cross. The sky-coverage gaps are the circles seen at lower center and (much distorted) at far upper left. For much of this orbit, the sunward camera is made unusable due to proximity of the Sun, either forcing the shutter to close or causing saturation. The prominent feature at upper left is an unusually bright instance of "SMEI aurora" occurring during passage through the northern polar cap. Kp equals 5 during this event but was as high as 8 in the previous 6 hours. The surface brightness of this phenomenon is about 200 ADU, greater than most of the Galactic plane.

Figure 3. Examples of the effect of aurora and charged-particle strikes on raw SMEI data frames. All are from the middle camera. a) A normal frame, taken 7 November 2004, 1554 UT, during a north polar cap passage. b) The same region of the sky two orbits later, showing

uniform elevated levels due to presence of aurora. c) A frame taken three minutes following the second, showing the granular effect of charged particle strikes on the CCD.

Figure 4. Sample all-sky orbit difference image, in a Hammer-Aitoff projection, showing a number of examples of SMEI aurora events and other features typically seen in the difference images. The data are from the period of intense geomagnetic activity in late October 2003; the start of the orbit is at 1137 UT 30 October. Kp equals 7 during this orbit. The various large-scale features demonstrate the instantaneous field of view of the three cameras; cf. Figure 1b. The orbital scanning motion is generally clockwise in the image. The numbers show the satellite's geographic latitude over the Earth at the time of the observation. The Sun is at the center, indicated by a cross. Ecliptic north is up, east to the left, and the antisunward direction is toward the extremes at either side.

Figure 5. Left: Example of a typical streamer event, with the observation commencing at 2156 UT 17 August 2003. Kp equals 5 during this event. The middle camera (right 2/3 of the image) and about half of the antisunward camera (left side) are shown; the sunward camera did not produce data in this time. The image is displayed in a simple cylindrical projection in which the scanning motion is rectilinear from bottom to top. The numbers to the right are the approximate geographic longitude and latitude, the direction of the center of the field of view (E of N), and the Universal Time. The vertical line represents the track of the negative velocity vector on the sidereal sky. The image covers about 90°×90° and represents a 20-minute period. A faint flash is seen at the bottom; at the top is another flash event followed by a zone of particle strikes on the CCD during crossing of the auroral oval. Note that for this figure, the reference image for the image differencing was the orbit image two orbits previous to this. Right: The same image

with the low spatial frequency component removed to show the filament structure. At least 10 filaments can be identified.

Figure 6. Correlation of SMEI aurora activity with the Ap/Kp index. a) Comparison of the Ap index (open histogram) and the SMEI Aurora Measure (filled histogram) during a geomagnetic storm in mid-June, 2003. b) The SAM for individual orbits plotted against the Kp index (dots). The crosses are the SAM averaged over each Kp bin. The solid line indicates an approximate lower-limit Kp value for a given SAM level. c) The probability of observing any SMEI aurora events during an orbit at a given Kp index value. The open histogram is for all SMEI aurora; the filled histogram is streamer events. There is a jump to >80% probability of observing some aurora activity in each orbit at about Kp equals 6.5.

Figure 7. Streamer event occurring almost exactly one orbit previous to the event shown in Figure 4, with the observation commencing at 2016 UT 17 August 2003. The projection and sky coverage are equivalent to that in Figure 4. Note that for both this figure and Figure 4, the reference image used for the image differencing was the orbit prior to this image.

Figure 8. Several examples of flash events showing structure on the trailing edge. The projection is similar to that for Figure 4; the scan direction is again bottom to top. In this case portions of both the sunward and antisunward cameras are included in addition to the middle camera. The total image sizes are about 120°×40° on the sidereal sky. Note that the upward bending toward the sides is an effect of the projection.

Figure 9. The location of the SMEI aurora flash events in magnetic local time and magnetic latitude, for the north cap region (a) and south (b). The distribution for streamer events is similar except that there is a much smaller percentage of nightside occurrences.

Figure 10. Two examples of fitting the vertical-column model, described in the text, to streamer events. Left: 4 January 2004, Kp equals 4. Right: 19 July 2003, Kp = 6. For each is shown the original streamer image, in a projection similar to that in Figure 4, covering about 90°×45° on the sidereal sky; the resulting outline contours of the best fit columns; and the locations and sizes of the columns in relation to the orbit track. In the latter, the columns are displayed as solid circles; structures assumed to cause the flash events in the images are displayed as open circles. The diameters of the model columns in these cases are 30–100 km, and the visible heights are ∼2000 km.

Figure 11. Streamer event for which the vertical column model provides a poor fit. The event is from 10 January 2004; Kp equals 5 during this period. The image is in a projection similar to Figure 4, and covers about 60°×60° on the sidereal sky; in this case only the middle camera is included. Clearly the streamer filaments converge to the left of the rearward vector track, which suggests that the physical structures may be canted or curved.

Figure 12. Streamer event observed to very low latitude, 27 July 2003. Kp equals 5 during this period, and reached 6 in the previous 6 hours. The projection is similar to that in Figure 4 and covers about 80°×110° on the sidereal sky. Note that the contrast has been adjusted differentially over the image to show detail, and so the grayscale levels are not a reliable indication of relative brightness. The SMEI aurora events, as described in the text, are: a bright (30 ADU) but typical streamer event at the bottom of the image, with the observation commencing about 0244 UT (1) and continuing for ∼10 minutes; a very bright (90 ADU) flash event at 0248 UT (2); and the low-latitude streamer event initially observed at 0250 UT (3) and continuing for ∼15 minutes down to a latitude of +20°. The low-latitude streamer filaments are much fainter than the earlier events, at most a few ADU. The granular appearance from 0252 UT (4) to 0258 UT (5) is a

Table 1. Statistics for SMEI aurora survey, 10 February 2003 to 10 February 2004.

Type	Flash	Streamer
Total	823	219
Northern hemisphere	488	136
Southern hemisphere	335	83
Dayside	450	182
Nightside	373	37
Median brightness (ADU)	4	9
Median duration (sec)	110	240
Median Kp index	4	5
Median magnetic latitude	73	74
Median MLT	13:00	12:20

Figure 6. Correlation of SMEI aurora activity with the Ap/Kp index. a) Comparison of the Ap index (open histogram) and the SMEI Aurora Measure (filled histogram) during a geomagnetic storm in mid-June, 2003. b) The SAM for individual orbits plotted against the Kp index (dots). The crosses are the SAM averaged over each Kp bin. The solid line indicates an approximate lower-limit Kp value for a given SAM level. c) The probability of observing any SMEI aurora events during an orbit at a given Kp index value. The open histogram is for all SMEI aurora; the filled histogram is streamer events. There is a jump to >80% probability of observing some aurora activity in each orbit at about Kp equals 6.5.

Figure 7. Streamer event occurring almost exactly one orbit previous to the event shown in Figure 4, with the observation commencing at 2016 UT 17 August 2003. The projection and sky coverage are equivalent to that in Figure 4. Note that for both this figure and Figure 4, the reference image used for the image differencing was the orbit prior to this image.

passage through the auroral oval. The angled shadow at upper right (6) is a coronal mass ejection (CME) here observed at a solar elongation of 60°. The band of speckles just prior to the CME (7) are star residuals due to a brief error in the satellite attitude determination.

Figure 13. The SMEI responsivity function R_λ.

Table 2. Individual star results for ADU-to-Rayleighs calibration. The spectral types and magnitudes were obtained from the SIMBAD database.

Star	Spectral Type	B Mag	V Mag	SMEI Flux (ADU Ster.)	Conversion R per ADU
α Lyr	A0V	0.03	0.03	0.837	36.9
Castor	A2V	1.63	1.59	0.211	35.3
Altair	A7V	0.97	0.75	0.486	36.6
Algol	B8V	2.07	2.12	0.123	35.8
HD 139006	A0V	2.24	2.21	0.108	38.4
α CMi	F5IV	0.74	0.34	0.792	37.2
β Tri	A5III	3.14	3.00	5.56×10^{-2}	38.7
α Eri	B3V	0.30	0.50	0.545	34.1
η Cen	B1V	2.17	2.32	9.14×10^{-2}	37.0
HD 103287	A0V	2.47	2.43	9.54×10^{-2}	35.5
η Oph	A2V	2.49	2.43	9.09×10^{-2}	37.8
β Dra	G2I	3.77	2.79	0.107	33.6
Canopus	F0II	-0.57	-0.72	1.86	36.4
θ Cen	K0III	3.07	2.06	0.218	37.1
Aldebaran	K5III	2.39	0.85	0.974	37.0
ϵ Cyg	K0III	3.49	2.50	0.165	32.6
Arcturus	K1.5III	1.19	-0.04	1.791	34.5
η Cas	B3III	3.22	3.34	4.12×10^{-2}	32.9
α Cyg	A2I	1.34	1.25	0.292	36.6
η UMa	B3V	1.76	1.85	0.143	37.5
Hamal	K2III	3.15	2.00	0.246	38.4
β Ari	A5V	2.77	2.64	7.66×10^{-2}	38.8
δ Cap	A7III	3.16	2.87	7.39×10^{-2}	34.2
α Ser	K2III	3.83	2.64	0.145	36.1
ζ Her	G0IV	3.54	2.89	9.08×10^{-2}	33.7
γ Cru	M3III	3.22	1.63	0.742	37.7
α Lup	B1.5III	2.13	2.28	0.100	34.9
α Phe	K0III	3.46	2.37	0.177	34.3
α Vir	B1III	0.91	1.04	0.321	34.1
α Lep	F0I	2.82	2.60	9.41×10^{-2}	35.6
β Leo	A3V	2.23	2.14	0.126	36.5
α Pyx	B1.5II	3.51	3.68	2.48×10^{-2}	39.3
β Crv	G5II	3.54	2.65	0.125	34.4
γ Gem	A0IV	1.93	1.90	0.142	38.9
β Lib	B8V	2.54	2.61	8.20×10^{-2}	34.4

Figure 11. Streamer event for which the vertical column model provides a poor fit. The event is from 10 January 2004; Kp equals 5 during this period. The image is in a projection similar to Figure 4, and covers about 60°×60° on the sidereal sky; in this case only the middle camera is included. Clearly the streamer filaments converge to the left of the rearward vector track, which suggests that the physical structures may be canted or curved.

Figure 12. Streamer event observed to very low latitude, 27 July 2003. Kp equals 5 during this period, and reached 6 in the previous 6 hours. The projection is similar to that in Figure 4 and covers about 80°×110° on the sidereal sky. Note that the contrast has been adjusted differentially over the image to show detail, and so the grayscale levels are not a reliable indication of relative brightness. The SMEI aurora events, as described in the text, are: a bright (30 ADU) but typical streamer event at the bottom of the image, with the observation commencing about 0244 UT (1) and continuing for ∼10 minutes; a very bright (90 ADU) flash event at 0248 UT (2); and the low-latitude streamer event initially observed at 0250 UT (3) and continuing for ∼15 minutes down to a latitude of +20°. The low-latitude streamer filaments are much fainter than the earlier events, at most a few ADU. The granular appearance from 0252 UT (4) to 0258 UT (5) is a passage through the auroral oval. The angled shadow at upper right (6) is a coronal mass ejection (CME) here observed at a solar elongation of 60°. The band of speckles just prior to the CME (7) are star residuals due to a brief error in the satellite attitude determination.

Figure 13. The SMEI responsivity function R_λ.

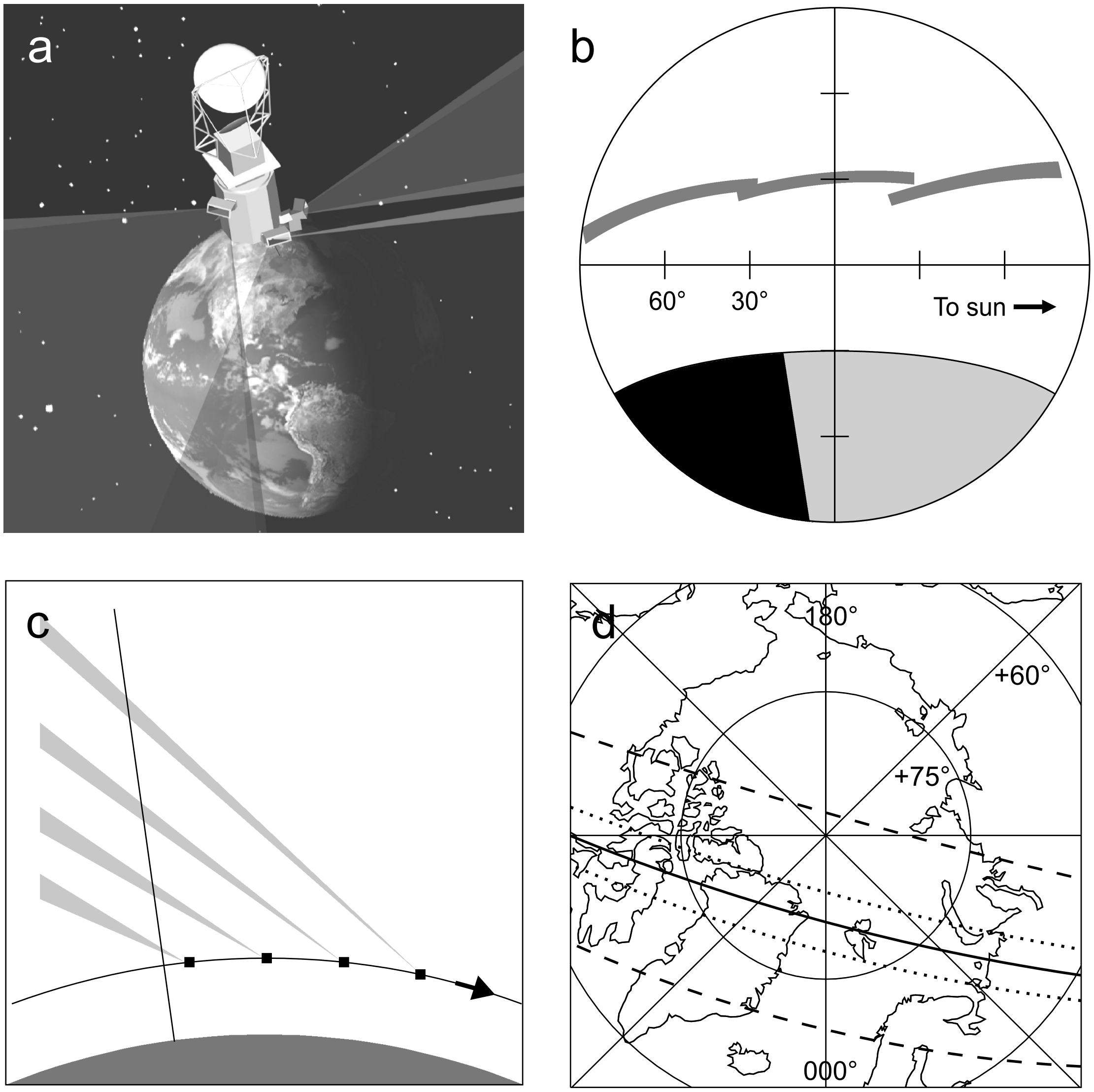

Figure 1. The geometry of the SMEI observations of the topside ionosphere. a) Schematic of the Coriolis satellite in orbit, showing how the SMEI cameras are mounted and the orientation of the fields of view. b) Schematic of the rearward-facing (negative velocity) hemisphere as seen from the satellite. Shown are the fields of view of the three cameras on the sky and the location of the Earth. The satellite orbit, nearly circular at an altitude of 840 km, follows approximately the terminator line. c) Schematic showing how the field of view of the SMEI cameras, over a given point over the Earth's surface, samples an increasing altitude with time. d) The sampling of the topside ionosphere for a single orbit track (solid line) crossing the northern polar cap. The dotted lines delineate the region sampled down to 1000 km (or lower) and the dashed lines delineate the region sampled down to 1500 km. About half the polar cap >60° is sampled from 1500 km on up during each orbit.

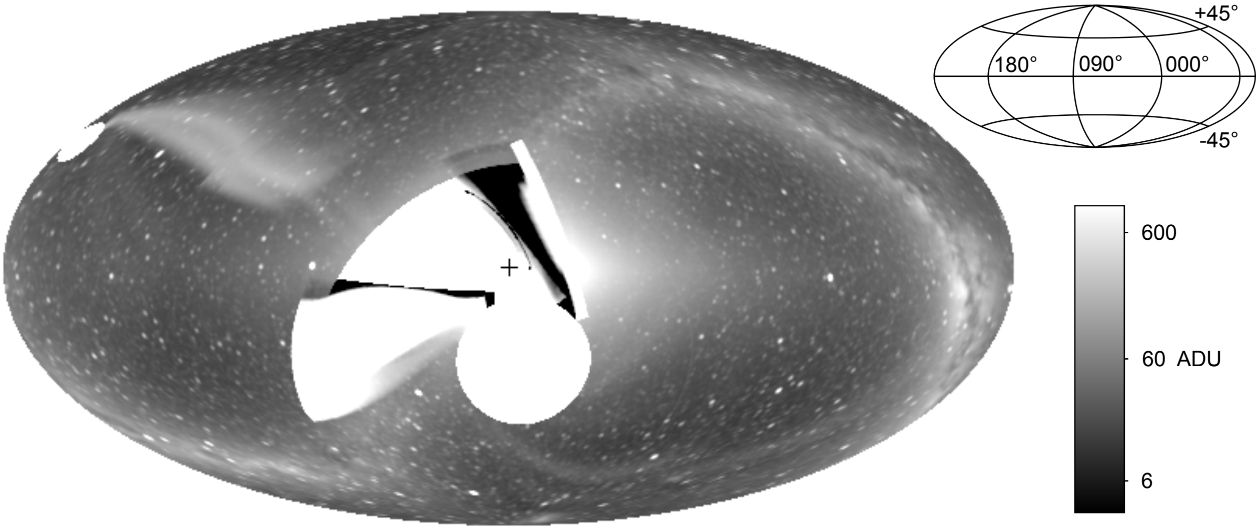

Figure 2. Example of an all-sky orbit image in a sun-centered Hammer-Aitoff projection, from 30 May, 2003, 0400-0541 UT. Ecliptic coordinates are displayed at upper right. The position of the Sun is indicated with a cross. The sky-coverage gaps are the circles seen at lower center and (much distorted) at far upper left. For much of this orbit, the sunward camera is made unusable due to proximity of the Sun, either forcing the shutter to close or causing saturation. The prominent feature at upper left is an unusually bright instance of "SMEI aurora" occurring during passage through the northern polar cap. Kp = 5 during this event but was as high as 8 in the previous 6 hours. The surface brightness of this phenomenon is about 200 ADU, greater than most of the Galactic plane.

Figure 3. Examples of the effect of aurora and charged-particle strikes on raw SMEI data frames. All are from the middle camera. a) A normal frame, taken 7 November 2004, 1554 UT, during a north polar cap passage. b) The same region of the sky two orbits later, showing uniform elevated levels due to presence of aurora. c) A frame taken three minutes following the second, showing the granular effect of charged particle strikes on the CCD.

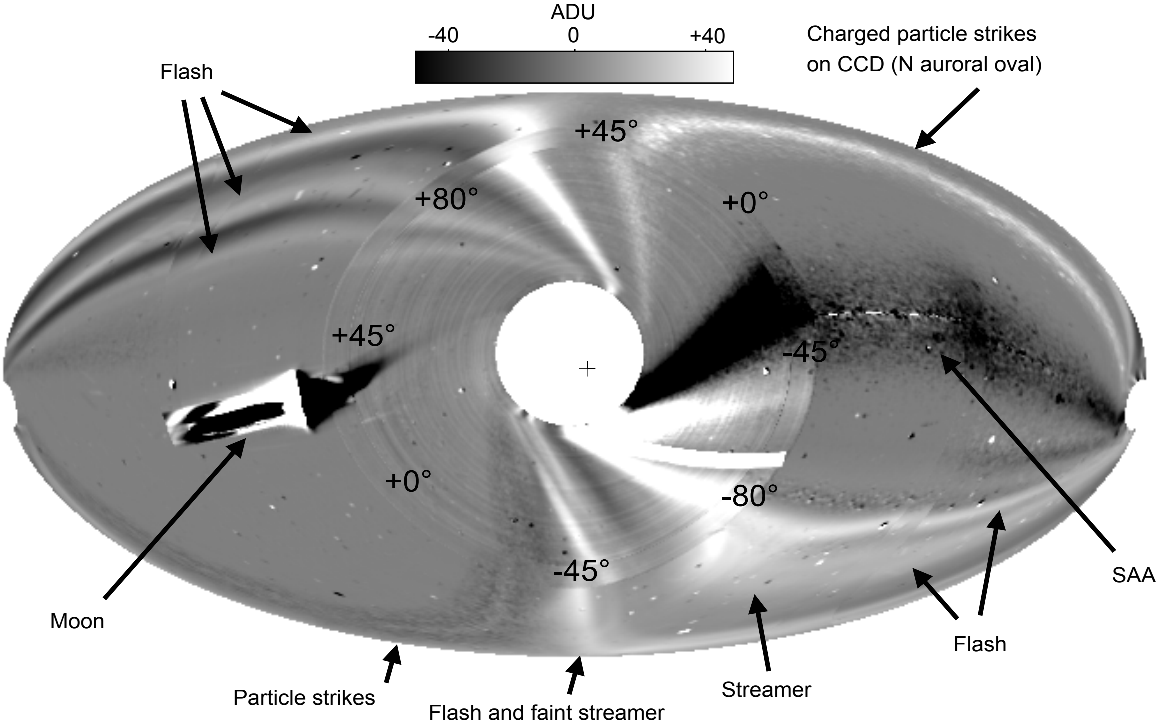

Figure 3. Sample all-sky orbit difference image, in a Hammer-Aitoff projection, showing a number of examples of SMEI aurora events and other features typically seen in the difference images. The data are from the period of intense geomagnetic activity in late October 2003; the start of the orbit is at 1137 UT October 30. Kp = 7 during this orbit. The various large-scale features demonstrate the instantaneous field of view of the three cameras; cf. Figure 1b. The orbital scanning motion is generally clockwise in the image. The numbers show the satellite's geographic latitude over the Earth at the time of the observation. The Sun is at the center, indicated by a cross. Ecliptic north is up, east to the left, and the antisunward direction is toward the extremes at either side.

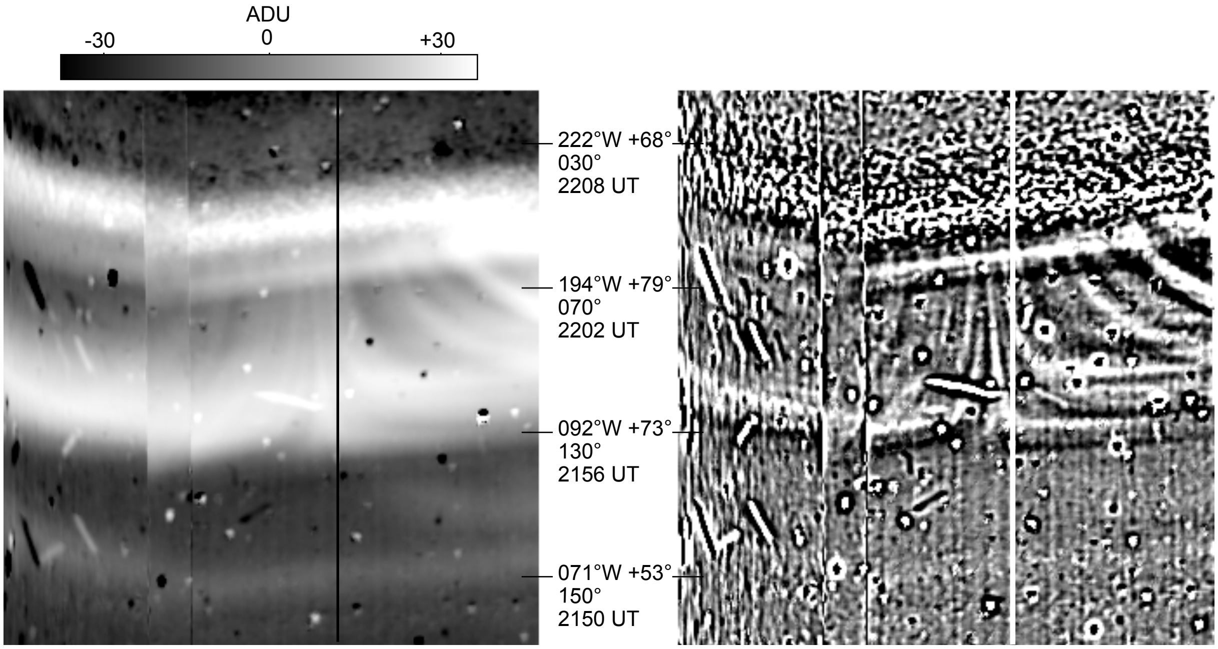

Figure 4. Left: Example of a typical streamer event, with the observation commencing at 2156 UT August 17, 2003. Kp = 5 during this event. The middle camera (right 2/3 of the image) and about half of the antisunward camera (left side) are shown; the sunward camera did not produce data in this time. The image is displayed in a simple cylindrical projection in which the scanning motion is rectilinear from bottom to top. The numbers to the right are the approximate geographic longitude and latitude, the direction of the center of the field of view (E of N), and the Universal Time. The vertical line represents the track of the negative velocity vector on the sidereal sky. The image covers about 90°×90° and represents a 20-minute period. A faint flash is seen at the bottom; at the top is another flash event followed by a zone of particle strikes on the CCD during crossing of the auroral oval. Note that for this figure, the reference image for the image differencing was the orbit image two orbits previous to this. Right: The same image with the low spatial frequency component removed to show the filament structure. At least 10 filaments can be identified.

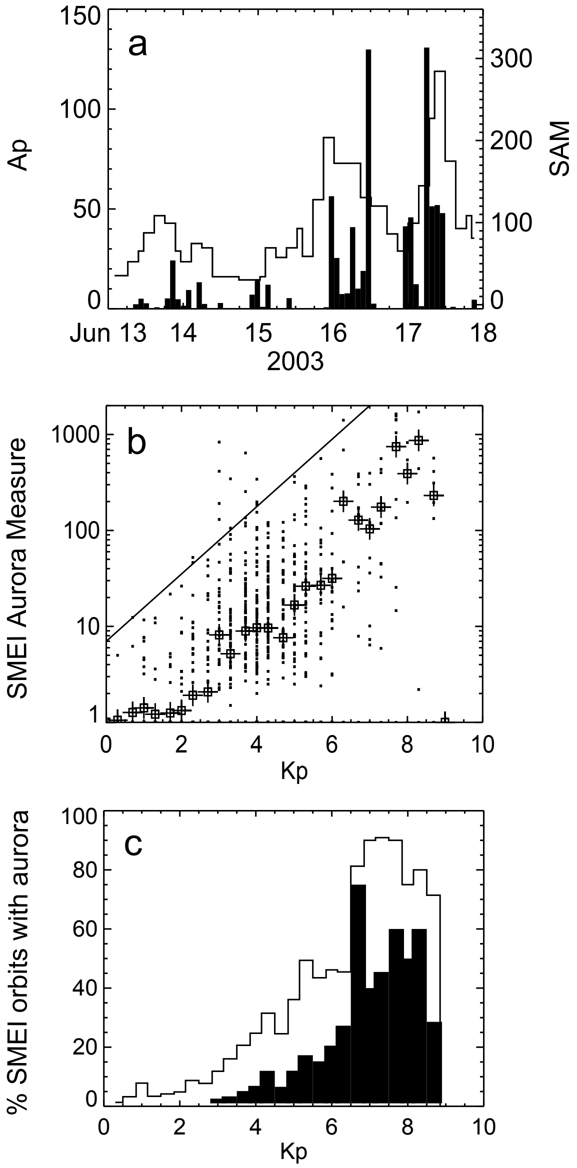

Figure 5. Correlation of SMEI aurora activity with the Ap/Kp index. a) Comparison of the Ap index (open histogram) and the SMEI Aurora Measure (filled histogram) during a geomagnetic storm in mid-June, 2003. b) The SAM for individual orbits plotted against the Kp index (dots). The crosses are the SAM averaged over each Kp bin. The solid line indicates an approximate lower-limit Kp value for a given SAM level. c) The probability of observing any SMEI aurora events during an orbit at a given Kp index value. The open histogram is for all SMEI aurora; the filled histogram is streamer events. There is a jump to >80% probability of observing some aurora activity in each orbit at about Kp = 6.5.

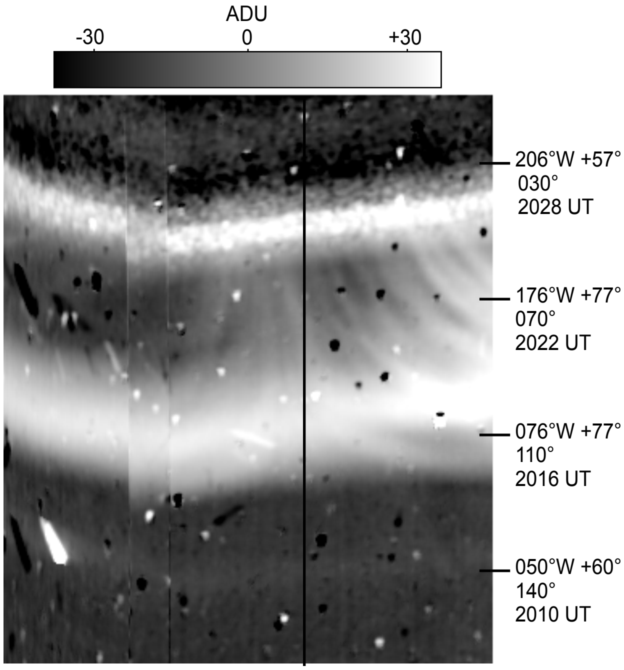

Figure 7. Streamer event occurring almost exactly one orbit previous to the event shown in Figure 4, with the observation commencing at 2016 UT August 17, 2003. The projection and sky coverage are equivalent to that in Figure 4. Note that for both this figure and Figure 4, the reference image used for the image differencing was the orbit prior to this image.

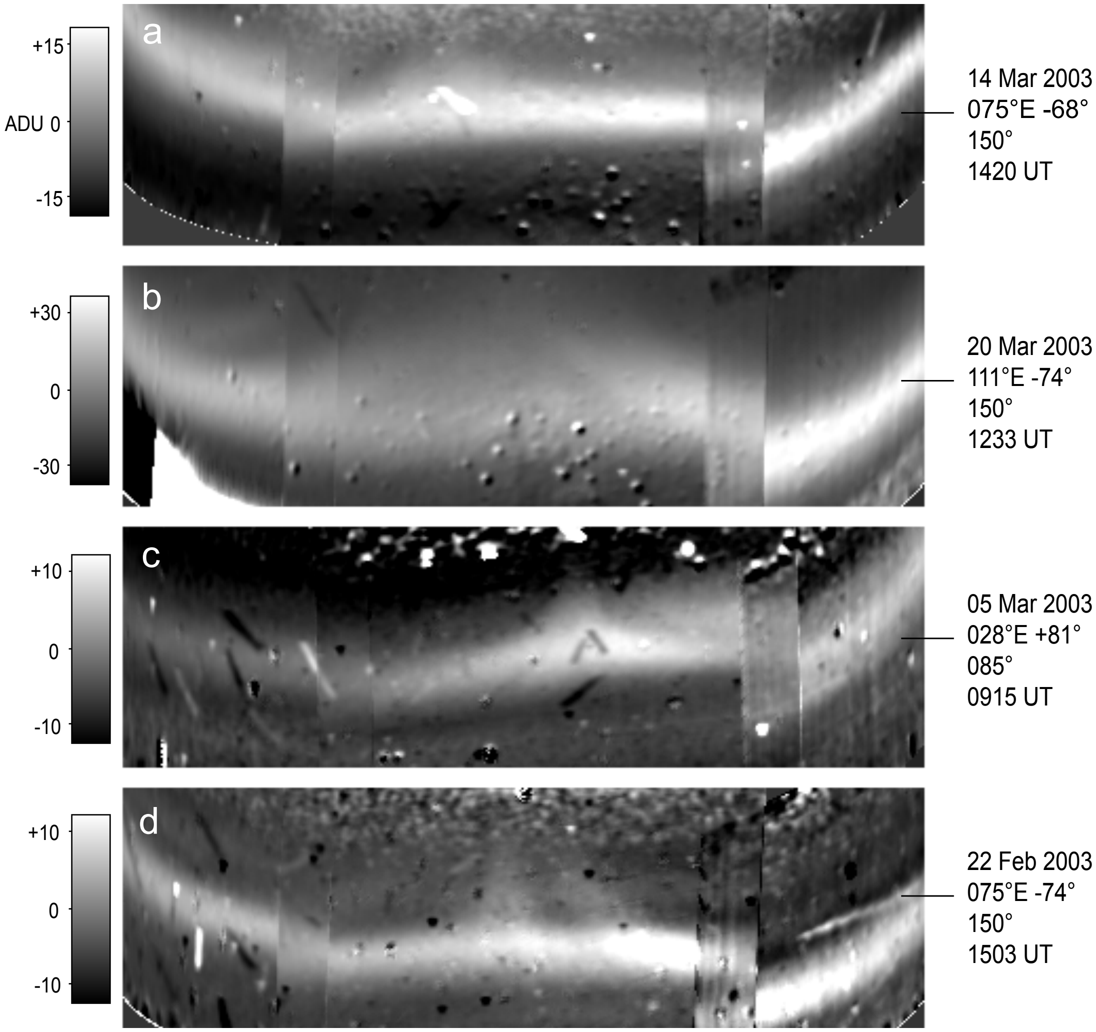

Figure 8. Several examples of flash events showing structure on the trailing edge. The projection is similar to that for Figure 4; the scan direction is again bottom to top. In this case portions of both the sunward and antisunward cameras are included in addition to the middle camera. The total image sizes are about 120°×40° on the sidereal sky. Note that the upward bending toward the sides is an effect of the projection.

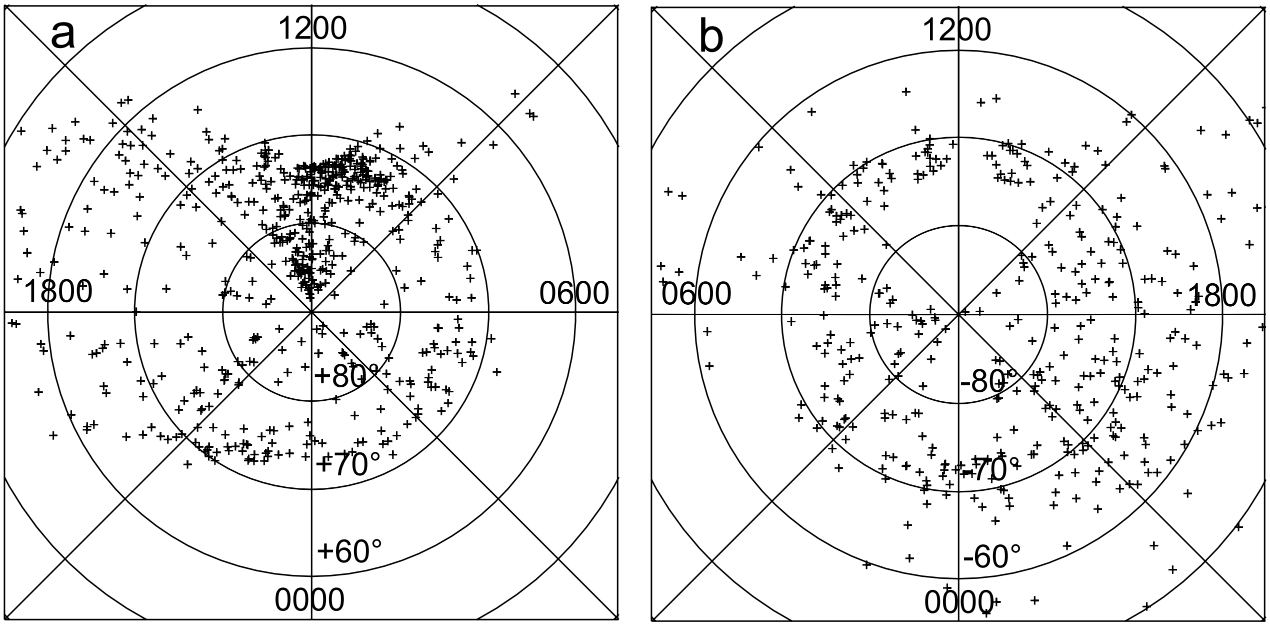

Figure 9. The location of the SMEI aurora flash events in magnetic local time and magnetic latitude, for the north cap region (a) and south (b). The distribution for streamer events is similar except that there is a much smaller percentage of nightside occurrences.

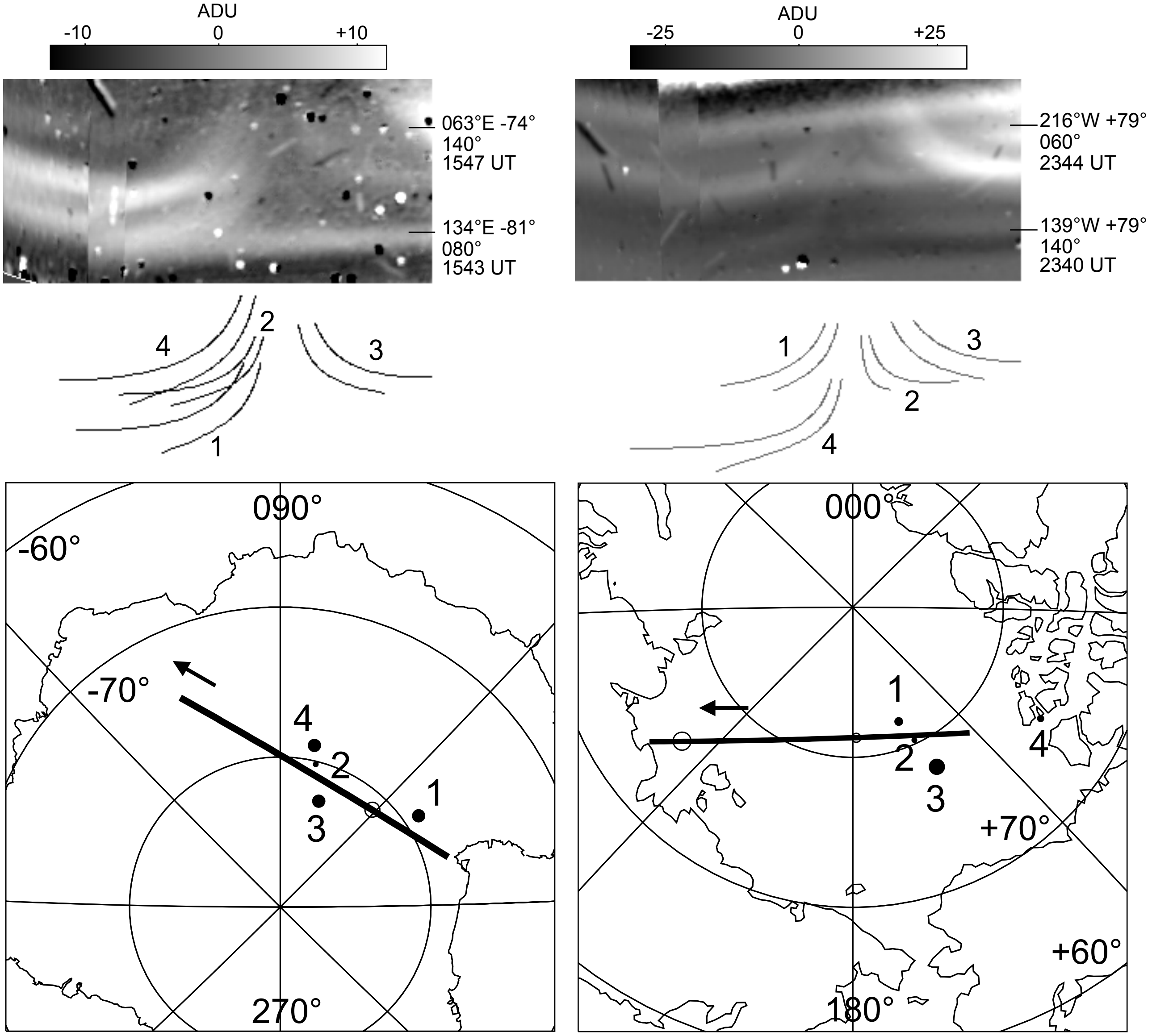

Figure 10. Two examples of fitting the vertical-column model, described in the text, to streamer events. Left: 4 January 2004, Kp = 4. Right: 19 July 2003, Kp = 6. For each is shown the original streamer image, in a projection similar to that in Figure 4, covering about 90°×45° on the sidereal sky; the resulting outline contours of the best fit columns; and the locations and sizes of the columns in relation to the orbit track. In the latter, the columns are displayed as solid circles; structures assumed to cause the flash events in the images are displayed as open circles. The diameters of the model columns in these cases are 30−100 km, and the visible heights are ~2000 km.

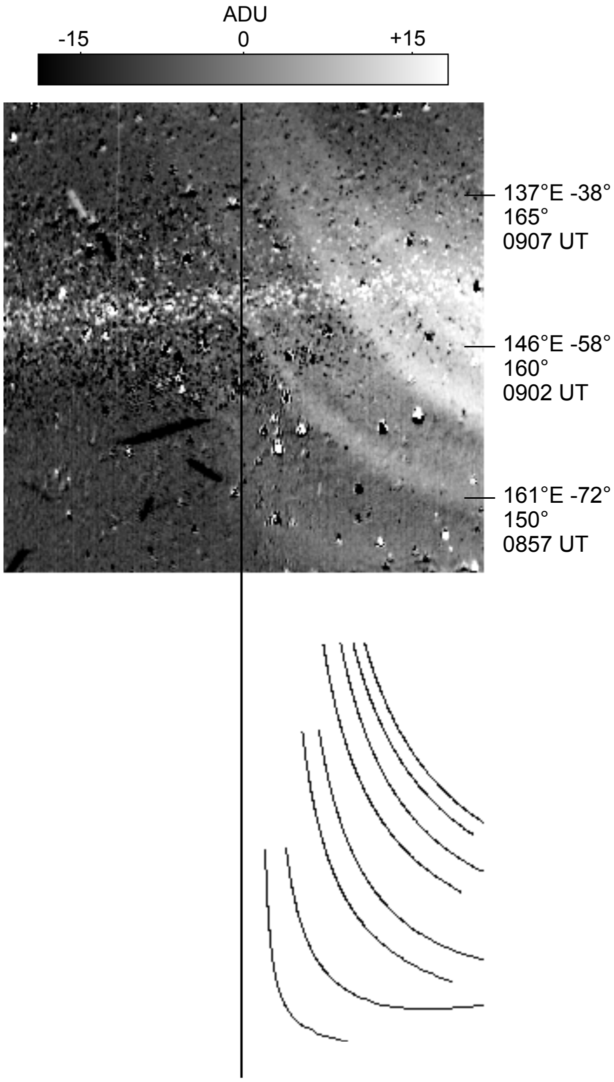

Figure 11. Streamer event for which the vertical column model provides a poor fit. The event is from 10 January 2004; Kp = 5 during this period. The image is in a projection similar to Figure 4, and covers about 60°×60° on the sidereal sky; in this case only the middle camera is included. Clearly the streamer filaments converge to the left of the rearward vector track, which suggests that the physical structures may be canted or curved.

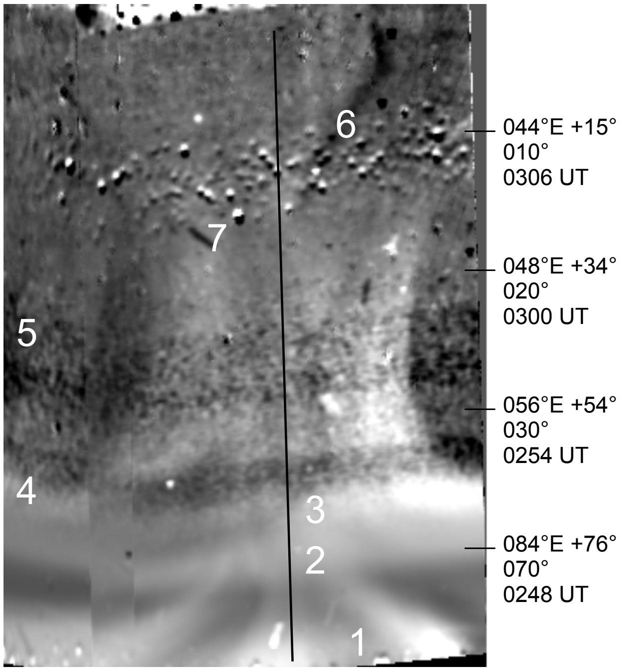

Figure 12. Streamer event observed to very low latitude, 27 July 2003. Kp = 5 during this period, and reached 6 in the previous 6 hours. The projection is similar to that in Figure 4 and covers about 80°×110° on the sidereal sky. Note that the contrast has been adjusted differentially over the image to show detail, and so the grayscale levels are not a reliable indication of relative brightness. The SMEI aurora events, as described in the text, are: a bright (30 ADU) but typical streamer event at the bottom of the image, with the observation commencing about 0244 UT (1) and continuing for ~10 minutes; a very bright (90 ADU) flash event at 0248 UT (2); and the low-latitude streamer event initially observed at 0250 UT (3) and continuing for ~15 minutes down to a latitude of +20°. The low-latitude streamer filaments are much fainter than the earlier events, at most a few ADU. The granular appearance from 0252 UT (4) to 0258 UT (5) is a passage through the auroral oval. The angled shadow at upper right (6) is a coronal mass ejection (CME) here observed at a solar elongation of 60°. The band of speckles just prior to the CME (7) are star residuals due to a brief error in the satellite attitude determination.

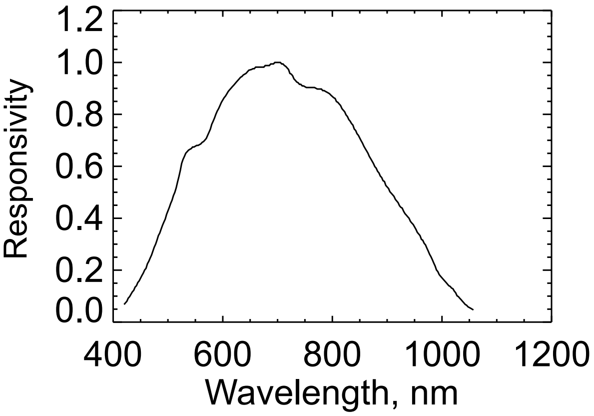

Figure 13. The SMEI responsivity function R_λ.